JOURNAL OF PETROLOGY

Journal of Petrology, 2021, Vol. 62, No. 12, 1–25
https://doi.org/10.1093/petrology/egab087
Advance Access Publication Date: 22 October 2021
Original Manuscript

OXFORD

Origin of Compositional Gradients with Temperature in the High-SiO_2 Rhyolite Portion of the Bishop Tuff: Constraints on Mineral–Melt–Fluid Reactions in the Parental Mush

Jameson S. R. Jolles* and Rebecca A. Lange

Department of Earth and Environmental Sciences, University of Michigan, Ann Arbor, MI 48109, USA

*Corresponding author. E-mail: jjolles@umich.edu

Received 3 September 2020; Revised 6 October 2021; Accepted 19 October 2021

Abstract

The Bishop Tuff (BT), erupted from the Long Valley caldera in California, displays two types of geochemical gradients with temperature: one is related to magma mixing, whereas the other is found in the high-SiO_2 rhyolite portion of the Bishop Tuff and is characterized by twofold or lower concentration variations in minor and trace elements that are strongly correlated with temperature. It is proposed that the latter zonation, which preceded phenocryst growth, developed as a result of mineral–melt partitioning between interstitial melt and surrounding crystals in a parental mush, from which variable melt fractions were segregated. To test this hypothesis, trends of increasing vs decreasing element concentrations with temperature (as a proxy for melt fraction), obtained from published data on single-clast pumice samples from the high-SiO_2 rhyolite portion of the Bishop Tuff, were used to infer their relative degrees of incompatibility vs compatibility between crystals and melt in the parental mush. Relative compatibility values (RCV_i) for all elements i, defined as the concentration slope with temperature divided by average concentration, are shown to be linearly correlated with their respective bulk partition coefficients (bulk D_i). Mineral–melt partition coefficients from the literature were used to constrain the average stoichiometry of the crystallization/melting reaction in the parental mush: 32 % quartz + 34 % plagioclase + 31 % K-feldspar + 1·60 % biotite + 0·42 % titanomagnetite + 0·34 % ilmenite + 0·093 % allanite + 0·024 % zircon + 0·025 % apatite = 100 % liquid. The proportions of tectosilicates in the reaction (i.e. location of eutectic) are consistent with depths of melt segregation of ~400–550 MPa and an activity of H_2O of ~0·4–0·6. Temperatures of <770–780 °C are constrained by allanite in the reaction. Evidence that a fluid phase was present in the parental mush is seen in the decreasing versus increasing H_2O and CO_2 contents with temperature in the segregated interstitial melt that formed the high-SiO_2 rhyolite portion of the Bishop Tuff. The presence of an excess fluid phase, which strongly partitions CO_2 relative to the melt, is required to explain the compatible behavior of CO_2, whereas the fluid abundance must have been low to explain the incompatible behavior of H_2O. Calculated degassing paths for interstitial melts, which segregated from the parental mush and ascended to shallower depths to grow phenocrysts, match published volatile analyses in quartz-hosted melt inclusions and constrain fluid abundances in the mush to be ≤1 wt%. The source of volatiles in the parental mush, irrespective of whether it formed by crystallization or partial melting, must have been primarily from associated basalts, as granitoid crust is too volatile poor. Approximately twice as much basalt as rhyolite is needed to provide the requisite volatiles. The determination of bulk D_i for several elements gives the bulk composition of the parental leucogranitic mush and shows that it is distinct from Mesozoic Sierran arc granitoids, as expected. Collectively, the results from this study provide new constraints for models of the complex, multi-stage processes throughout the

Plio-Quaternary, involving both mantle-derived basalt and pre-existing crust, that led to the origin of the parental body to the Bishop Tuff.

Key words: volatiles; partition coefficient; high-silica rhyolite; compositional gradients; Bishop Tuff

INTRODUCTION

High-silica rhyolites are the most differentiated magmas on Earth and are the product of some of the largest explosive eruptions. An example is the climactic eruption of the Bishop Tuff from Long Valley caldera (Fig. 1), where >600 km^3 of compositionally zoned rhyolite (77–74 wt% SiO_2) were erupted in <1 week (Wilson & Hildreth, 1997; Hildreth & Wilson, 2007) at ~765 ka (Andersen *et al.*, 2017). One of the defining features of the Bishop Tuff, first identified by Hildreth (1977, 1979), is evidence for systematic co-variations in temperature and composition in the magma prior to eruption, the origins of which have been widely debated. Understanding the development of these gradients may clarify the key processes that led to the accumulation and explosive eruption of such a large volume of highly differentiated rhyolite.

In concert with compositional and temperature co-variations, there are also systematic changes in the mineralogy of the Bishop rhyolite. Most (not all) pumice clasts erupted to the south and east of Long Valley caldera contain nine mineral phases (quartz + sanidine + plagioclase + biotite + titanomagnetite + ilmenite + zircon + apatite + allanite), whereas most (not all) clasts erupted to the north contain the same assemblage (minus allanite) as well as two pyroxenes, monazite, and pyrrhotite, along with Ba-rich sanidine rims and Ti-rich quartz rims (e.g. Hildreth, 1977; Hervig & Dunbar, 1992; Peppard *et al.*, 2001; Hildreth & Wilson, 2007). These mineralogical distinctions led Evans *et al.* (2016) to propose two criteria to categorize Bishop pumices as Early or Late: (1) absence or presence of Ba-rich sanidine rims and (2) absence or presence of pyroxene. As emphasized by Hildreth (2017), these two mineralogical criteria cannot be used to infer the timing of eruptive units. Therefore, in this study the terms Early-type and Late-type are used to be consistent with established nomenclature applied to the Bishop Tuff (e.g. Hildreth, 1977, 1979), without drawing inferences about the timing within the multi-day eruptive sequence of the Bishop Tuff. The term Transitional-type, introduced by Chamberlain *et al.* (2015), is applied to pumice clasts that contain at least some sanidine with Ba-rich rims, but no pyroxene.

Importantly, there are two completely different types of geochemical gradients with temperature in the Bishop Tuff. In Late-type pumices, the compositionally distinct rims on quartz (Ti-rich) and sanidine (Ba-rich) have been attributed to magma mixing between a high-SiO_2 rhyolite, from which the cores of quartz and sanidine crystallized, and a variety of differentiated melts with less SiO_2 (e.g. Hervig & Dunbar, 1992; Peppard *et al.*, 2001; Hildreth & Wilson, 2007). These Late-type pumices are additionally characterized by abrupt and large increases in whole-rock MgO, CaO, Ba, and Sr contents over a narrow temperature interval (≤25 degrees; Hildreth, 1977; Hildreth & Wilson, 2007; Jolles & Lange, 2019).

The second type of geochemical zonation with temperature is seen in the high-SiO_2 rhyolite portion of the Bishop Tuff, which constitutes more than two-thirds of the erupted volume (≥400 km^3; Hildreth & Wilson, 2007), and includes both Early- and Transitional-type pumices. This chemical zonation is defined by continuous and large (twofold or lower) changes in whole-rock trace-element concentrations as a linear function of temperature (≤50 degrees), in the absence of any systematic changes in whole-rock SiO_2 content (e.g. Hildreth, 1979; Jolles & Lange, 2019). It has long been concluded that these temperature and geochemical gradients preceded phenocryst growth in the high-SiO_2 rhyolite portion of the Bishop Tuff (e.g. Hildreth, 1979, 2017; Hildreth & Wilson, 2007; Jolles & Lange, 2019). It is the origin of this geochemical zonation with temperature, which preceded phenocryst growth, that is the focus of this study.

Although the occurrence of Ba-rich rims on some sanidine crystals in Transitional-type samples (a criterion for its classification; Evans *et al.*, 2016) raises the possibility that some of this chemical zonation with temperature in the high-SiO_2 rhyolite portion of the Bishop Tuff may also be due to mixing with less differentiated magmas, albeit to a lesser extent than seen in Late-type samples, similar twofold variations in trace-element concentrations (e.g. 154–306 ppm Rb; 32–15 ppm La) are found in Glass Mountain (GM) high-SiO_2 rhyolites (Metz & Mahood, 1991), which erupted prior to the Bishop Tuff (Fig. 1). In the GM rhyolites, these twofold variations are accompanied by extremely low concentrations of Sr (<3 ppm; Davies *et al.*, 1994; Davies & Halliday, 1998), which precludes mixing with less differentiated magma that contains even modest amounts of Sr (e.g. >10 ppm).

An alternative hypothesis to explain the twofold variations in trace-element concentrations in these high-SiO_2 rhyolites, which is unrelated to magma mixing, involves variable melt segregation from a granitic crystal-rich mush (Metz & Mahood, 1991; Hildreth, 2004, 2017; Hildreth & Wilson, 2007), where different melt fractions have a different trace-element composition. As noted by Wolff *et al.* (2015), the specific pattern of chemical gradients in various minimum/eutectic rhyolites observed in the rock record, including the Early-type Bishop Tuff, is consistent with differentiation mechanisms that involve mineral–melt partition coefficients predicted from the observed phenocryst assemblage in each respective deposit.

In this study, we quantitatively evaluate whether all element concentration gradients with temperature in the high-SiO_2 rhyolite portion of the Bishop Tuff can be explained by segregation of different interstitial melt fractions from a granitic crystal-rich mush that contains the same nine phenocryst phases as found in Early- and Transitional-type Bishop samples. If so, we examine whether an average stoichiometry of the crystallization/melting reaction in the parental mush can be deduced. We additionally evaluate if gradients in the volatile contents (H_2O and CO_2) with temperature across the Bishop Tuff allow the composition and relative abundance of a fluid phase during segregation of variable melt fractions to be determined. Finally, we address whether constraints can be placed on the bulk composition of the parental mush.

ELEMENT COMPATIBILITY/INCOMPATIBILITY IN INTERSTITIAL HIGH-SiO_2 RHYOLITE MELT RELATIVE TO CRYSTAL-RICH MUSH

If the high-SiO_2 rhyolite portion of the Bishop Tuff is derived from the segregation of variable melt fractions of interstitial melt from a

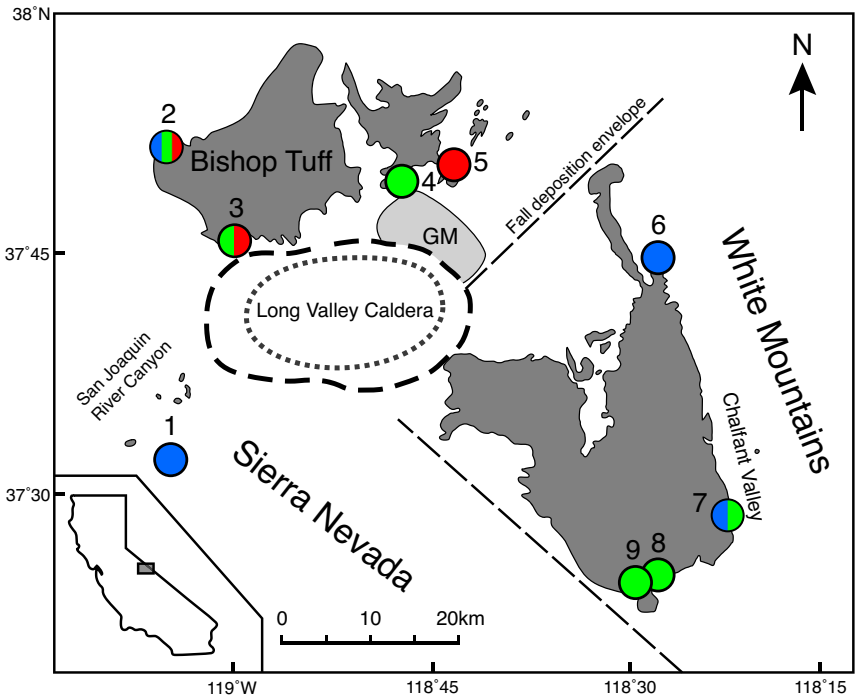

Fig. 1. Bishop Tuff and Long Valley caldera, California, adapted from Chamberlain *et al.* (2015). Glass Mountain (GM) in light grey. Sample locations of Early- (blue), Transitional- (green), and Late-type (red) Bishop pumices: 1, San Joaquin River drainage; 2, Aeolian Buttes; 3, Crestview; 4, Wild Cow Canyon; 5, McGee Canyon; 6, Blind Spring Hill; 7, Chalfant Quarry; 8, Chalk Bluffs; 9, Pleasant Valley Dam.

crystal-rich mush (e.g. Hildreth, 2004, 2017), trends of increasing vs decreasing minor- and trace-element concentration with temperature can be used to infer the respective degree of incompatibility vs compatibility for all elements between the bulk of all crystals present and the interstitial melt, under three broad assumptions: (1) equilibrium crystallization/melting; (2) temperature as a proxy for melt fraction (and/or source depletion); (3) a broadly homogeneous parental mush, with the same crystal phases present (although modal abundances can vary). We demonstrate the viability of these three assumptions below.

Equilibrium (vs fractional) crystallization/melting to describe interstitial melt in crystal-rich mush

There are two endmember processes by which interstitial melts develop in a crystal-rich mush: (1) extensive crystallization of a parental liquid or (2) partial melting of a parental pluton. An intermediate process between these two endmembers is partial melting of cumulates (e.g. Wolff *et al.*, 2015). In the case of crystallization, Dufek & Bachmann (2010) showed that melt segregation is optimized at 50–70 % crystallization, for compaction to allow melt extraction. As a consequence, geochemical models based on closed-system equilibrium crystallization more closely approximate the conditions in a crystal-rich mush at the time of melt segregation than models based on open-system Rayleigh fractional crystallization. Moreover, because melt evolution during equilibrium crystallization and equilibrium partial melting is modeled by the same equation, its application to infer the geochemical evolution of an interstitial melt in a crystal-rich mush applies equally to a melt that formed by extensive crystallization or partial melting. The equilibrium crystallization/melting equation is

$$\frac{C_i^{\mathrm{liq}}}{C_i^{\mathrm{parent}}} = \frac{1}{\left(F + D_i^{\mathrm{bulk}} - FD_i^{\mathrm{bulk}}\right)} \quad (1)$$

where C_i^{liq} is the concentration of element i in the interstitial liquid, C_i^{parent} is the initial concentration of element i in the bulk parent, F is the melt fraction, and D_i^{bulk} is the bulk partition coefficient for element i between the interstitial melt and the crystallizing/melting mineral assemblage.

Temperature as a proxy for melt fraction (and/or source depletion)

Under equilibrium crystallization (or equilibrium partial melting) conditions, the concentration of an element in the interstitial melt (within a crystal-rich mush) will vary as a function of two factors: (1) its bulk partition coefficient; (2) melt fraction. Figure 2 schematically illustrates this relationship. For elements that are strongly compatible (i.e. bulk partition coefficients >1), their concentration strongly increases as a function of melt fraction. If temperature can be used as a proxy for melt fraction (and/or source depletion), elements with concentrations in the high-SiO_2 rhyolite portion of the Bishop Tuff that strongly increase (or decrease) with increasing temperature may be interpreted as having bulk partition coefficients, between all crystals and interstitial melt in the parental mush, that are strongly compatible (or incompatible). Similarly, elements with concentrations that are constant with temperature can be inferred to have bulk partition coefficients that are close to ~1.

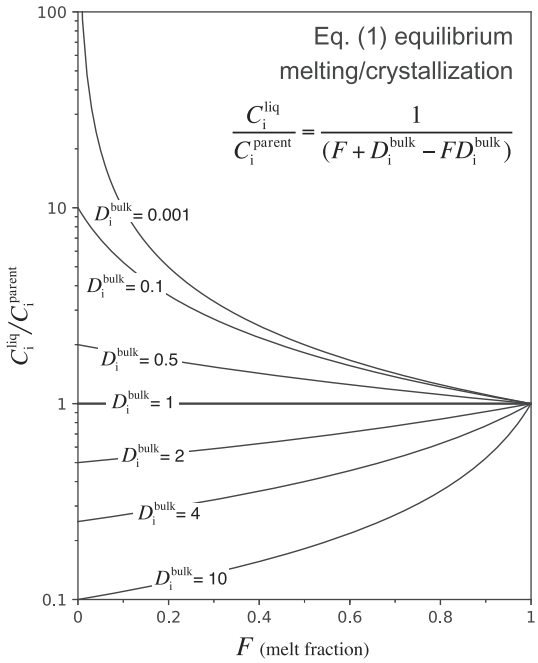

Fig. 2. Equilibrium crystallization/melting diagram for various melt fractions (F) and partition coefficients (D), where C_i^{liq}/C_i^{parent} represents the concentration of an element in the liquid (C_i^{liq}) relative to the parental source (C_i^{parent}), following equation (1). It should be noted that for elements with $D < 1$, concentration in the liquid will decrease with increasing melt fraction. Conversely, for elements with $D > 1$, concentration in the liquid will increase with increasing melt fraction. Elements with a $D \sim 1$ will see no change in concentration in the liquid with increasing melt fraction.

The schematic illustration in Fig. 2 shows that under the assumption that temperature is a proxy for melt fraction (and/or source depletion), trace-element concentration gradients with temperature can be used to infer not only which elements are compatible (positive slopes) and incompatible (negative slopes), but also how the elements rank, relative to one another, in degree of compatibility and incompatibility. By constraining the relative degrees of compatibility/incompatibility for key elements, tight constraints on the stoichiometry of the crystallization/melting reaction in the granitic crystal-rich mush (from which the high-SiO_2 rhyolite portion of the Bishop Tuff was extracted) can be obtained from two pieces of information: (1) slopes of element concentration with temperature in Early/Transitional-type Bishop pumices; (2) element partition coefficients between high-SiO_2 rhyolite melt and the nine mineral phases in Early Bishop pumices.

BISHOP TUFF: SAMPLE LOCATIONS AND GEOCHEMICAL GRADIENTS WITH TEMPERATURE

The single-clast pumice samples from the Bishop Tuff (Fig. 1) that are used in this study are those previously described and studied by Jolles & Lange (2019). Six are Early-type and five are Transitional-type. Another 12 are Late-type, which are shown for comparison only. To obtain major- and trace-element compositions of whole-rock single-clast pumices, samples (crystals and matrix) were crushed by hand using a ceramic mortar and pestle and powdered in a tungsten carbide shatterbox. Samples were then analyzed by inductively coupled plasma mass spectrometry (ICP-MS) at Activation Laboratories Ltd, Ontario, Canada. Samples are mixed with lithium metaborate and lithium tetraborate fluxes and fused in an induction furnace. The resulting melt is completely dissolved in a 5 % nitric acid solution with an internal standard and then run on an ICP-MS system. Compositions for Early- and Transitional-type single clasts are reported in Tables 1 and 2, whereas those for Late-type clasts are given in Supplementary Table 1, Supplementary Data, Electronic Appendix 1 (supplementary data are available for downloading at http://www.petrology.oxfordjournals.org). Standards employed and the precision for all analyzed elements are reported in Supplementary Table 2, Supplementary Data, Appendix 1.

The high-resolution Fe–Ti oxide temperatures (± 3–12 degrees) and oxygen fugacity (relative to the Ni–NiO buffer; ΔNNO) results, obtained for each sample by Jolles & Lange (2019) with the thermometer/oxybarometer of Ghiorso & Evans (2008), are reported in Table 1. It should be noted that for each single-clast pumice sample, the crushed material was split in two, with one half used for whole-rock analysis and the other half for Fe–Ti oxide analyses (Jolles & Lange, 2019). The Fe–Ti oxide temperatures for the 23 single-clast samples are strongly correlated ($R^2 = 0{\cdot}94$) to those obtained with the two-feldspar thermometer of Putirka (2008) on the same clasts (Jolles & Lange, 2019), which underscores their accuracy. From the combined temperature, fO_2, and whole-rock compositional data, the melt ferric–ferrous ratio in each sample can be calculated using the model of Kress & Carmichael (1991); the resulting Fe_2O_3 and FeO wt% values are listed in Table 1.

High-SiO_2 rhyolite endmember to Late-type Bishop Tuff samples

The focus in this study is on the high-SiO_2 rhyolite portion of the Bishop Tuff, namely the Early- and Transitional-type samples. Late-type samples are not included because of ample evidence that they were affected by magma mixing (e.g. Hervig & Dunbar, 1992; Hildreth & Wilson, 2007; Roberge *et al.*, 2013; Chamberlain *et al.*, 2015), which masks the trace-element pattern owing to segregation of variable melt fractions from a parental mush. It should be noted, however, that previous studies (Hildreth & Wilson, 2007; Chamberlain *et al.*, 2014, 2015; Evans *et al.*, 2016; Hildreth, 2017; Jolles & Lange, 2019) concluded that the high-SiO_2 rhyolite endmember in Late-type samples, which mixed with less differentiated melts, was slightly hotter than Transitional-type high-SiO_2 rhyolite and thus reflects a continuation to higher temperatures of the thermal and compositional zoning seen in the high-SiO_2 rhyolite melts that form the Early- and Transitional-type samples. Therefore, the high-SiO_2 rhyolite endmember to the Late-type samples will at times be referred to in this study, but the Late-type samples themselves will not be employed.

Volatile gradients

Jolles & Lange (2019) reported wt% H_2O values calculated from the plagioclase–liquid hygrometer of Waters & Lange (2015) when combined with the Fe–Ti oxide temperatures. The resulting H_2O contents decrease systematically with increasing temperature (Fig. 3a), which is consistent with the fluid-saturated (H_2O–CO_2) phase-equilibrium results from Klimm *et al.* (2008) at 200 MPa. The results from that study show that the temperature of the liquidus surface for co-crystallization of quartz–sanidine–plagioclase increases with decreasing water content in the melt phase (Fig. 3b). The H_2O contents from Jolles & Lange (2019) are also consistent with those

Table 1: Whole-rock major- and minor-element (wt%) concentrations and temperatures (°C) for Early- and Transitional-type single clast samples

Sample:	BT-15D	BT-15A	BT-16B	BT-22B	BT-22A	BT-16A	BT-13A	BT-24D	BT-8B	BT-19D	BT-21C
Unit:	F7	F7	Ig2Ea	Ig1Eb	Ig1Eb	Ig2Ea	Ig2Ea	Ig1Eb	Ig2Eb	Ig2NWb	Ig2NWa
Pumice type:	Early	Early	Early	Early	Early	Early	Trans.	Trans.	Trans.	Trans.	Trans.
Lat. (37°N):	27·583	27·583	27·583	44·595	44·595	27·583	24·829	27·646	24·838	51·463	45·832
Long. (118°W):	22·124	22·124	22·124	27·272	27·272	22·124	31·449	21·986	30·874	64·525	59·875
SiO_2	76·52	77·25	77·44	77·95	77·06	77·73	77·19	77·6	78·06	77·54	74·71
TiO_2	0·07	0·07	0·07	0·07	0·07	0·08	0·09	0·09	0·10	0·12	0·13
Al_2O_3	13·34	12·66	12·42	12·25	12·83	12·55	12·41	12·75	11·94	12·43	14·65
FeO^T	0·75	0·78	0·78	0·69	0·73	0·75	0·80	0·78	0·83	0·79	1·03
FeO*	0·60	0·62	0·62	0·56	0·57	0·59	0·62	0·61	0·64	0·61	0·80
Fe_2O_3*	0·17	0·18	0·18	0·15	0·18	0·18	0·20	0·19	0·20	0·20	0·26
MnO	0·037	0·036	0·035	0·035	0·032	0·033	0·029	0·031	0·030	0·028	0·030
MgO	0·11	0·10	0·07	0·07	0·05	0·11	0·12	0·12	0·10	0·10	0·10
CaO	0·52	0·52	0·51	0·51	0·48	0·56	0·62	0·52	0·56	0·63	0·57
Na_2O	3·35	3·32	3·80	3·52	3·86	3·31	3·29	3·68	3·38	3·00	2·84
K_2O	5·29	5·25	4·89	4·92	4·88	4·87	5·43	4·44	4·99	5·32	5·93
P_2O_5	0·01	0·01	< 0·01	< 0·01	< 0·01	0·02	0·01	< 0·01	< 0·01	0·03	0·02
LOI	4·91	6·28	3·00	2·76	3·47	3·36	2·94	4·43	2·38	2·58	3·83
Total	99·2	98·4	100·0	100·8	99·8	98·4	99·0	98·4	100·3	99·2	99·3
Fe^{3+}/Fe^{T}*	0·201	0·202	0·200	0·201	0·222	0·213	0·228	0·220	0·231	0·228	0·229
Fe–Ti *T* (°C)†	698	703	706	713	728	729	734	739	742	748	752
Prop. err. (°C)‡	±11	±6	±3	±8	±12	±12	±6	±12	±7	±6	±5
H_2O (wt%)§	7·2	6·8	6·8	6·6	6·3	6·2	5·7	6·2	5·5	5·4	5·8

Trans., Transitional. Major-element analyses normalized to 100 %. LOI and original totals also shown. Estimated 2σ precisions (based on replicate ICP-MS analyses on standards) are ≤2 % for MgO and CaO; ≤3 % for SiO_2, TiO_2, FeO^T, FeO, Fe_2O_3, Na_2O, and K_2O; <4 % for Al_2O_3; and ≤8 % for MnO.

*Determined using model of Kress & Carmichael (1991).

†Fe–Ti oxide temperatures from Jolles & Lange (2019), based on geothermometer of Ghiorso & Evans (2008).

‡Propagated analytical error in temperature from Jolles & Lange (2019).

§Calculated H_2O concentrations in melt during phenocryst growth from Jolles & Lange (2019), based on plagioclase–liquid hygrometer of Waters & Lange (2015).

analyzed in quartz-hosted melt inclusions (MIs; Wallace *et al*., 1999; Anderson *et al*., 2000; Roberge *et al*., 2013; Myers *et al*., 2019), where the Early-type (cooler) Bishop samples record higher water contents than the Late-type (hotter) samples (Fig. 3c). It should be noted that these studies also show the inverse behavior for CO_2, with concentrations increasing from Early-type (cooler) to Late-type (hotter) samples (Fig. 3d). In the Late-type samples (unit Ig2NWa), melt inclusions in the Ti-poor quartz cores (crystallized from a high-SiO_2 rhyolite endmember prior to mixing) contain up to ~500 ppm CO_2 (Roberge *et al*., 2013), whereas those in quartz phenocrysts from Early-type samples (unit F6) contain ≤170 ppm CO_2 (Anderson *et al*., 2000). Therefore, the melt inclusion data show that CO_2 contents increase with melt temperature in the high-SiO_2 rhyolite portion of the Bishop Tuff.

Major-element gradients

The four major, anhydrous oxide components in the Bishop rhyolite are SiO_2, Al_2O_3, Na_2O, and K_2O, and they are plotted as a function of Fe–Ti oxide temperature for 23 single-clast pumice samples in Fig. 4. Consistent with previous work (Hildreth, 1977), SiO_2 contents are high and unchanging (78–76 wt%) in the Early- and Transitional-type samples (with one exception; BT-21C) and are zoned (76–73 wt%) in Late-type samples. Al_2O_3 contents follow a similar but reversed pattern; they are relatively low and unchanging (~12–13 wt%) in the Early- and Transitional-type samples (with one exception; BT-21C) and are zoned to higher values (~13–16 wt%) in Late-type samples. Na_2O and K_2O contents also show an inverse pattern with temperature relative to one another, with Na_2O contents consistently higher in Early- and Transitional-type samples than in Late-type samples and K_2O contents displaying the opposite pattern (Fig. 4c and d).

Minor-element gradients

Whole-rock concentrations of the minor elements (TiO_2, MgO, CaO, Fe_2O_3, and FeO) in the high-SiO_2 rhyolite portion of the Bishop Tuff are plotted as a function of Fe–Ti oxide temperature for 23 single-clast pumice samples. TiO_2 contents are unchanging in Early-type rhyolite, but increase linearly among Transitional- and Late-type samples (Fig. 5a). MgO, CaO, and Fe_2O_3 contents all gradually increase with temperature in Early- and Transitional-type rhyolite, and sharply increase in Late-type samples (Fig. 5b–d). In contrast, the FeO content varies little with temperature in the high-SiO_2 rhyolite portion of the Bishop Tuff (Fig. 5e), although it increases in Late-type pumices. Also shown is the increase in Fe^{3+}/Fe^T with temperature

Table 2: Whole-rock trace-element (ppm) concentrations for Early- and Transitional-type single clast samples

Sample:	BT-15D	BT-15A	BT-16B	BT-22B	BT-22A	BT-16A	BT-13A	BT-24D	BT-8B	BT-19D	BT-21C
Unit:	F7	F7	Ig2Ea	Ig1Eb	Ig1Eb	Ig2Ea	Ig2Ea	Ig1Eb	Ig2Eb	Ig2NWb	Ig2NWa
Pumice type:	Early	Early	Early	Early	Early	Early	Trans.	Trans.	Trans.	Trans.	Trans.
Ba	14	12	8	16	16	23	35	40	29	118	108
Sr	10	10	6	6	6	14	18	18	12	32	27
Rb	190	189	189	187	169	168	150	144	153	117	131
Zr	92	66	72	73	79	79	83	85	92	89	126
Nb	18	15	15	18	13	15	12	16	12	9	15
Hf	3·4	2·8	3·0	3·1	2·8	2·7	2·9	3·1	2·8	2·8	3·4
Ta	2·5	2·5	2·7	2·5	2·1	2·1	1·8	1·8	1·7	1·7	1·8
Cs	5·5	5·9	6·2	5·9	4·9	5·2	4·2	4·0	4·1	2·9	3·4
Th	21·8	20·7	20·8	21·0	20·0	19·2	16·5	16·7	17·6	15·4	16·5
U	7·5	7·5	7·4	7·5	6·7	6·5	5·7	5·0	5·4	4·2	4·7
Mn	287	279	271	271	248	256	225	240	232	217	235
Y	31	29	27	27	26	23	21	17	20	13	19
La	23·3	18·8	22·8	21·7	27·0	26·3	35·3	31·7	43·7	59·3	41·8
Ce	50·3	42·2	50·2	47·3	55·7	55·8	66·5	62·0	86·0	105·6	88·6
Pr	5·76	4·93	5·60	5·45	6·21	5·86	7·17	6·32	8·52	9·93	7·70
Nd	19·0	16·7	19·1	18·4	20·1	19·5	22·1	19·9	25·8	28·7	22·2
Sm	4·1	3·9	4·1	4·0	4·3	3·8	3·9	3·7	4·3	4·0	3·2
Eu	0·06	0·05	0·05	0·05	0·07	0·05	0·08	0·07	0·10	0·14	0·15
Gd	3·6	3·6	3·7	3·6	3·4	3·4	3·1	2·8	3·1	2·6	2·6
Tb	0·6	0·7	0·6	0·6	0·5	0·5	0·4	0·5	0·4	0·4	0·4
Dy	4·0	3·7	3·6	3·8	3·5	3·4	2·8	2·8	2·9	2·3	2·3
Ho	0·7	0·8	0·7	0·8	0·7	0·6	0·5	0·5	0·5	0·4	0·5
Er	2·3	2·4	2·3	2·4	2·2	2·0	1·8	1·7	1·7	1·3	1·5
Tm	0·37	0·33	0·41	0·41	0·32	0·32	0·31	0·28	0·31	0·22	0·24
Yb	2·8	2·6	2·4	2·5	2·4	2·2	1·9	1·8	1·8	1·3	1·6
Lu	0·42	0·43	0·41	0·41	0·38	0·32	0·31	0·28	0·31	0·23	0·24

Trans., Transitional. Estimated 2σ precisions (based on replicate ICP-MS analyses of standards) are ≤2 % for Ba; ≤3 % for Sr; ≤5 % for Ta; ≤6 % for U and Yb; ≤8 % for Nb, Th, Mn, Ce, and Lu; ≤9 % for Y, La, Pr, Nd, Sm, Eu, Gd, Tb, Dy, and Tm; ≤10 % for Rb, Cs, Ho, and Er; ≤12 % for Lu; ≤13 % for Hf; ≤17 % for Zr.

(Fig. 5f), which reflects the increase in oxygen fugacity (relative to the Ni–NiO buffer) with increasing temperature, as revealed by the application of the Fe–Ti oxide thermometer/oxybarometer (Ghiorso & Evans, 2008) to analyzed pairs of titanomagnetite and ilmenite (Jolles & Lange, 2019).

Trace-element gradients

The rare earth element (REE) concentrations (the lanthanides and yttrium) are plotted as a function of Fe–Ti oxide temperature in Fig. 6. The concentrations of La, Ce, Pr, Nd, and Eu all increase with temperature (Fig. 6a–d) whereas Sm is unchanging with temperature. Conversely, the concentrations of Gd, Tb, Yb, Lu, and Y all decrease with temperature (Fig. 6e–i). Importantly, the magnitude of the slopes (i.e. REE concentrations with temperature) systematically vary from the lightest to heaviest REE, with La contents increasing the most (twofold increase from Early- to Transitional-type) and Y contents decreasing the most (twofold decrease from Early- to Transitional-type). Europium, as expected, falls off this trend because it occurs in two valence states (2+ and 3+), and its slope of concentration with temperature is between those for the two lightest REE (La and Ce; Fig. 6). Among the remaining nine trace elements that are plotted, the concentrations of Ba, Sr, and Zr increase with temperature (Fig. 7a–c), and the remaining six (Hf, Mn, Rb, Ta, Th, and U) decrease with temperature (Fig. 7e–h). It should be noted that Mn is a trace element in the Bishop rhyolite, owing to ≤300 ppm concentrations (Table 2).

Linear fits of trace-element concentrations with temperature, among the high-SiO_2 rhyolite portion of the Bishop Tuff, display remarkably strong correlations, irrespective of whether concentrations increase (e.g. $R^2 = 0{\cdot}72$ for Ce) or decrease (e.g. $R^2 = 0{\cdot}87$–$0{\cdot}92$ for Rb, U, Th, Lu, Ta, and Mn) with temperature. Whether the strong correlations between element concentration and temperature can be used to determine element compatibility vs incompatibility between an interstitial melt and the surrounding multi-mineral assemblage in a parental mush is evaluated below. If so, these strong linear correlations indicate that the parental mush was broadly homogeneous in its bulk composition and mineral assemblage.

RELATIVE COMPATIBILITY VALUES (RCV)

For each element in Figs 4–7, the slope of its concentration with temperature was divided by the average concentration to obtain its 'relative compatibility value' (RCV: Table 3). For this analysis, only high-SiO_2 single-clast samples were used (all Early-type and all but one Transitional-types; Tables 1 and 2). One Transitional-type sample was excluded owing to its lower SiO_2 content (BT-21C; Jolles & Lange, 2019), as well as all Late-type samples, for the reason that they may have been affected by magma mixing.

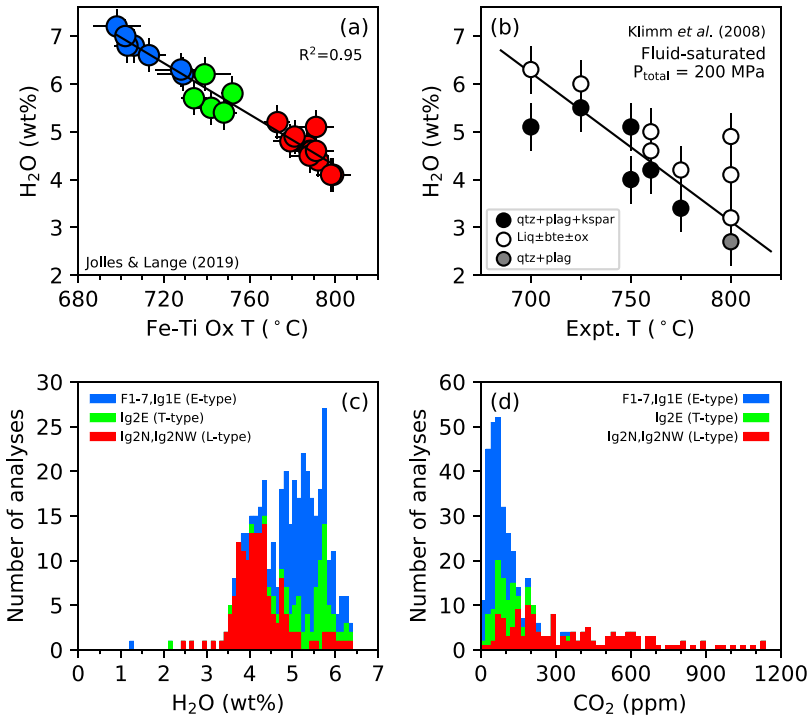

Fig. 3. (a) Plagioclase–liquid hygrometry results for Early-, Transitional-, and Late-type Bishop single clast pumices vs Fe–Ti oxide temperature (°C). Error bars (2σ) in water (y-axis) are propagated from the uncertainty in temperature (x-axis) reported by Jolles & Lange (2019). (b) Experimental phase equilibria data from Klimm *et al*. (2008) for a high-SiO_2 rhyolite with constant pressure (P_{total} = 200 MPa) but varying activity of H_2O. Line designates the quartz + plagioclase + K-feldspar cotectic. (c, d) Histograms (stacked) of (c) H_2O (wt%) and (d) CO_2 (ppm) for literature melt-inclusion data from F1–F7 and Ig1Eb units (blue; Early-type), Ig2E (green; Transitional-type), and Ig2N and Ig2NW (red; Late-type) units of the Bishop Tuff. Studies referenced include Wallace *et al*. (1999), Anderson *et al*. (2000), Roberge *et al*. (2013), Myers *et al*. (2019).

Major elements

The anhydrous major oxide components in the high-SiO_2 rhyolite portion of the Bishop Tuff are SiO_2, Al_2O_3, Na_2O, and K_2O. In all cases, their concentration gradients with temperature are close to zero, which means that their RCVs (slopes divided by average concentration) are also near zero. This pattern is consistent with invariant behavior (little change in melt composition with melt fraction), which is expected for near-eutectic melts in the Quartz (Qz)–Plagioclase (Pl)–K-feldspar (Kfs) system.

Minor elements

The relative compatibility values (RCVs) for the five minor elements (Table 3) in the high-SiO_2 rhyolite portion of the Bishop Tuff shows that the order of compatibility is $Ti > Fe^{3+} > Mg \sim Ca > Fe^{2+}$. Importantly, Ti has a relative compatibility that is nearly three times larger than that for Fe^{3+}, which in turn is nearly three times larger than that for Fe^{2+}. The two alkaline earth cations, Mg and Ca, are similarly compatible to each other and to Fe^{3+}. The slope for Fe^{2+} (FeO component) is close to zero, which implies a bulk partition coefficient that is close to one. The increase in the Fe^{3+}/Fe^{T} ratio with temperature (Fig. 5f), therefore, reflects the higher compatibility of Fe^{3+} relative to Fe^{2+}.

Trace elements

The RCVs for the REE (Table 3) show that the order of compatibility broadly follows their order on the periodic table, with La > Ce > Pr > Nd > Sm > Tb > Dy > Lu > Yb > Y. Europium, as expected, deviates from this trend because it occurs in two valence states (2+ and 3+). Its relative compatibility is intermediate between La and Ce, and all three are strongly compatible. It should be noted that Sm has a flat slope (RCV close to zero), which indicates a bulk partition coefficient of ~1. The relative compatibility of the two heaviest lanthanides, Lu and Yb (both strongly incompatible), are switched relative to their position on the periodic table, but are nonetheless similar. Finally, Y has equal incompatibility to Yb and thus these are the most incompatible of the REE.

Among the remaining trace elements, the order of compatibility is Ba > Sr > Zr > Hf > Mn > Th > Rb > Ta ~ U. Barium and Sr are the most strongly compatible of all the trace elements, whereas Zr is only moderately compatible. The two actinides, Th and U, are both highly incompatible, as is the alkali Rb. Uranium and Ta are nearly as incompatible as Y and Yb, and these four trace elements are the most incompatible of all elements in the Bishop high-SiO_2 rhyolite.

Volatile components

The concentration of dissolved H_2O in the high-SiO_2 rhyolite portion of the Bishop Tuff decreases linearly with increasing temperature (Fig. 3a), which indicates that it behaved as an incompatible component in the crystallizing/melting parental mush. In contrast, melt inclusion data show that the concentration of dissolved CO_2 increases with temperature, consistent with compatible behavior (Fig. 3d). This contrasting pattern for H_2O and CO_2 (incompatible and compatible, respectively) points to the presence of an excess fluid phase in the crystallizing/melting granitoid mush during melt segregation, otherwise both dissolved volatiles would behave incompatibly

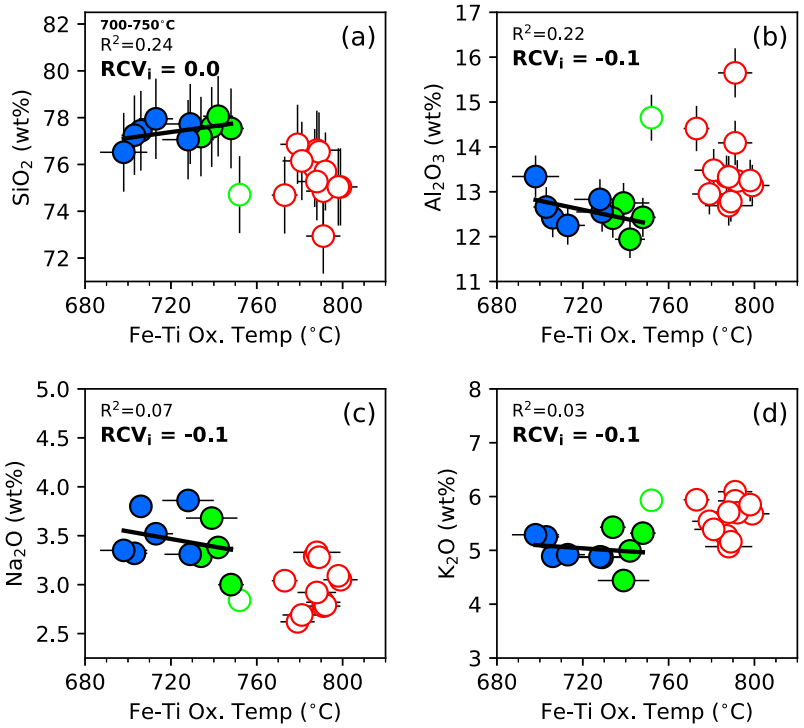

Fig. 4. Major-element variations (wt%) with Fe–Ti oxide temperature (°C). Values are relatively unchanging for the Early- (blue) and Transitional-type (green) samples, as denoted by RCV_i (relative compatibility values) close to zero. It should be noted that one Transitional-type sample (BT-21C), shown as an open symbol, is not included in the RCV_i calculation owing to its SiO_2 less than 75 wt%. Late-type Bishop pumices are shown as red open symbols and are not included in any RCV_i calculations. RCV for each component is calculated from the concentration slope with temperature, divided by the average concentration (see text). Error bars represent 2σ uncertainty (see text).

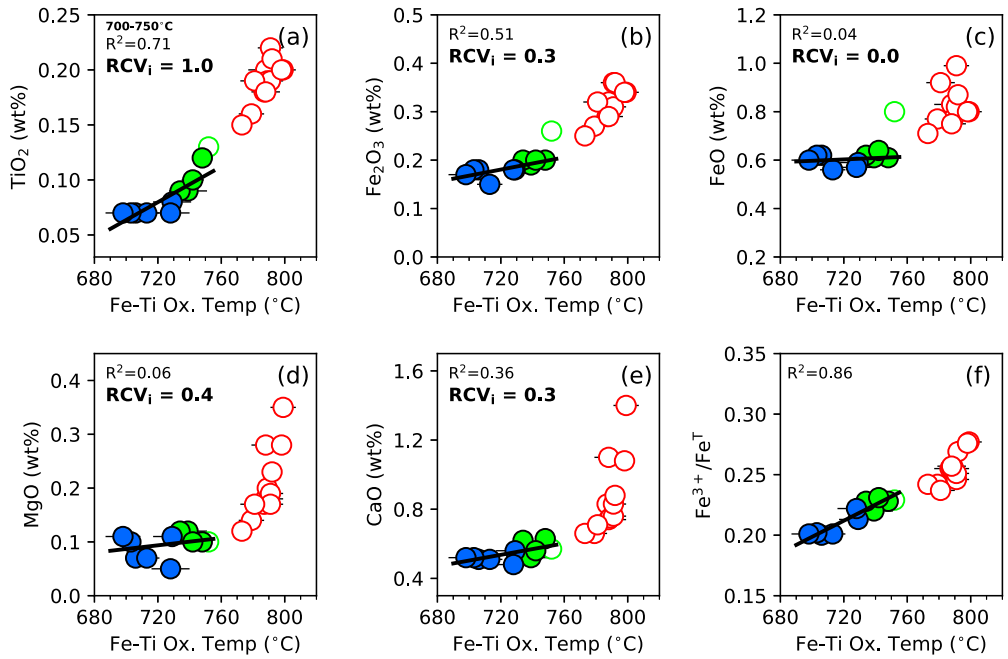

Fig. 5. Minor-element (wt%) and Fe^{3+}/Fe^{T} variations with Fe–Ti oxide temperature (°C). TiO_2, Fe_2O_3, MgO, and CaO all increase with temperature and are compatible. However, FeO $RCV_i \sim 0$, suggesting no change in concentration with temperature. Fe^{3+}/Fe^{T} also increases with temperature, reflecting the increase in oxygen fugacity (relative to the Ni–NiO buffer) with temperature. Colors and symbols same as in Fig. 4.

(both would decrease with increasing temperature). Therefore, a fluid phase that strongly partitions CO_2 relative to the melt must have been present for CO_2 to behave compatibly in the parental mush. Because H_2O is also partitioned into a fluid phase relative to melt, but not as strongly as CO_2 (owing to the much lower solubility of CO_2 relative to H_2O in rhyolite melts), the overall mass abundance of the fluid

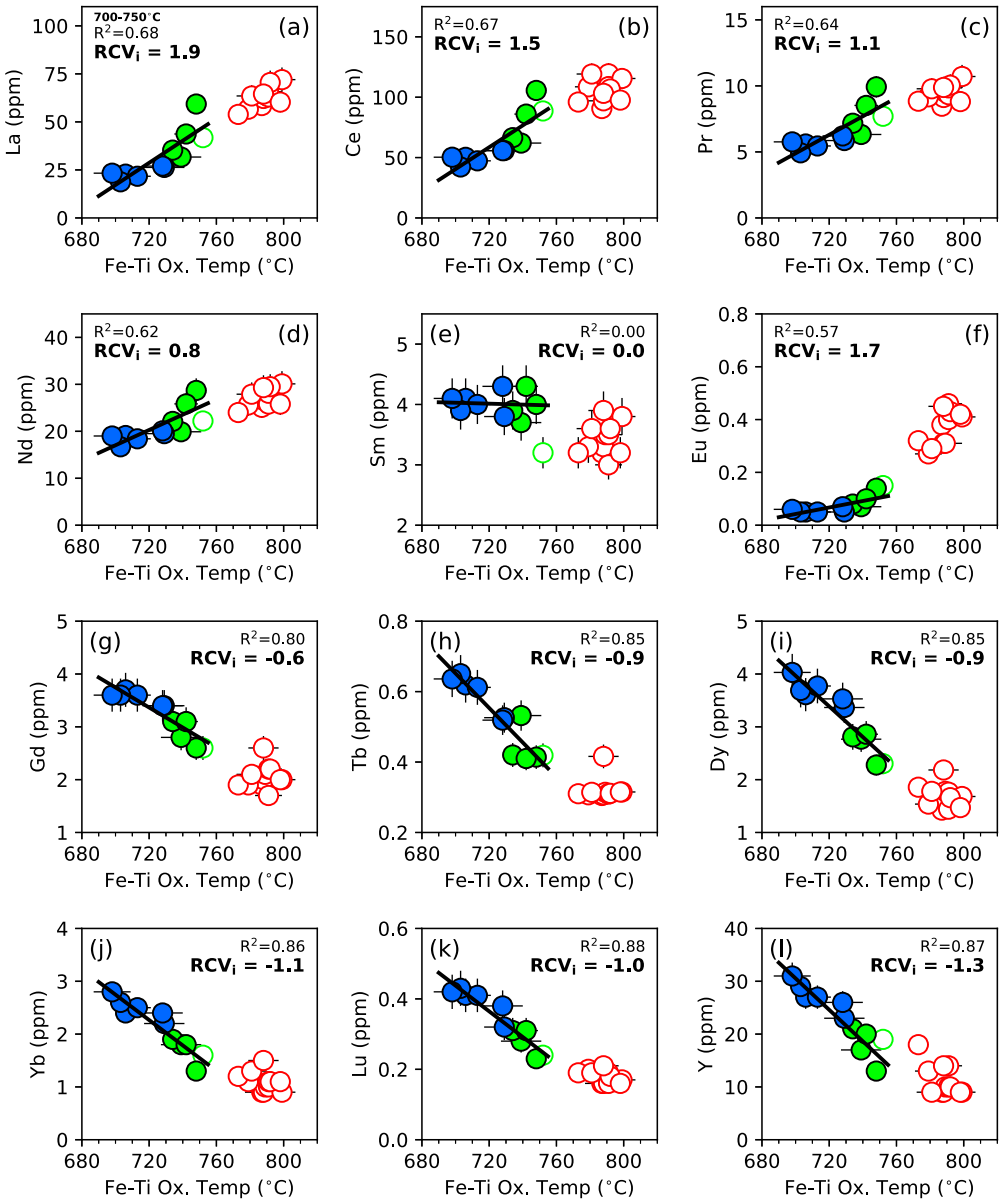

Fig. 6. Rare earth element (REE) variations (ppm) with Fe–Ti oxide temperature (°C). It should be noted that REE lighter than Sm have $RCV_i > 0$ and are compatible, and REE (except Eu) heavier than Sm have $RCV_i < 0$, and are incompatible. Sm $RCV_i \sim 0$, with concentration unchanging with temperature. Colors and symbols same as in Fig. 4.

phase during crystallization/melting in the granitoid mush must have been small enough that the bulk partition coefficient was less than one for H_2O (i.e. incompatible) but greater than one for CO_2 (i.e. compatible).

MINERAL–MELT PARTITION COEFFICIENTS

To convert the relative compatibility values (RCVs) for each element (Table 3) into bulk partition coefficients (by constraining the stoichiometry of the crystallization/melting reaction in the parental mush), mineral–melt partition coefficients are needed for the nine mineral phases in Early-type (high-SiO_2 rhyolite) Bishop samples. Because element partition coefficients may vary strongly as a function of melt and/or mineral composition, only those determined for the nine mineral phases from Early-type (high-SiO_2 rhyolite) Bishop samples are used in this study.

Allanite, zircon, and apatite

For the trace-element partition coefficients, the results from Mahood & Hildreth (1983) on the Early-type Bishop Tuff are used for allanite (Aln) and zircon (Zrn) on the basis of instrumental neutron activation analysis (INAA) of mineral separates and coexisting glass shards; the results are summarized in Table 3. Mahood & Hildreth (1983) did not report partition coefficient results for apatite (Ap), and therefore high-resolution microprobe analyses of La, Ce, Nd, Sm, Dy, and Y were obtained in this study on apatite crystals in Early-type pumice clasts from Jolles & Lange (2019). Details regarding the analysis of apatite are provided in Electronic Appendix 2. Apatite

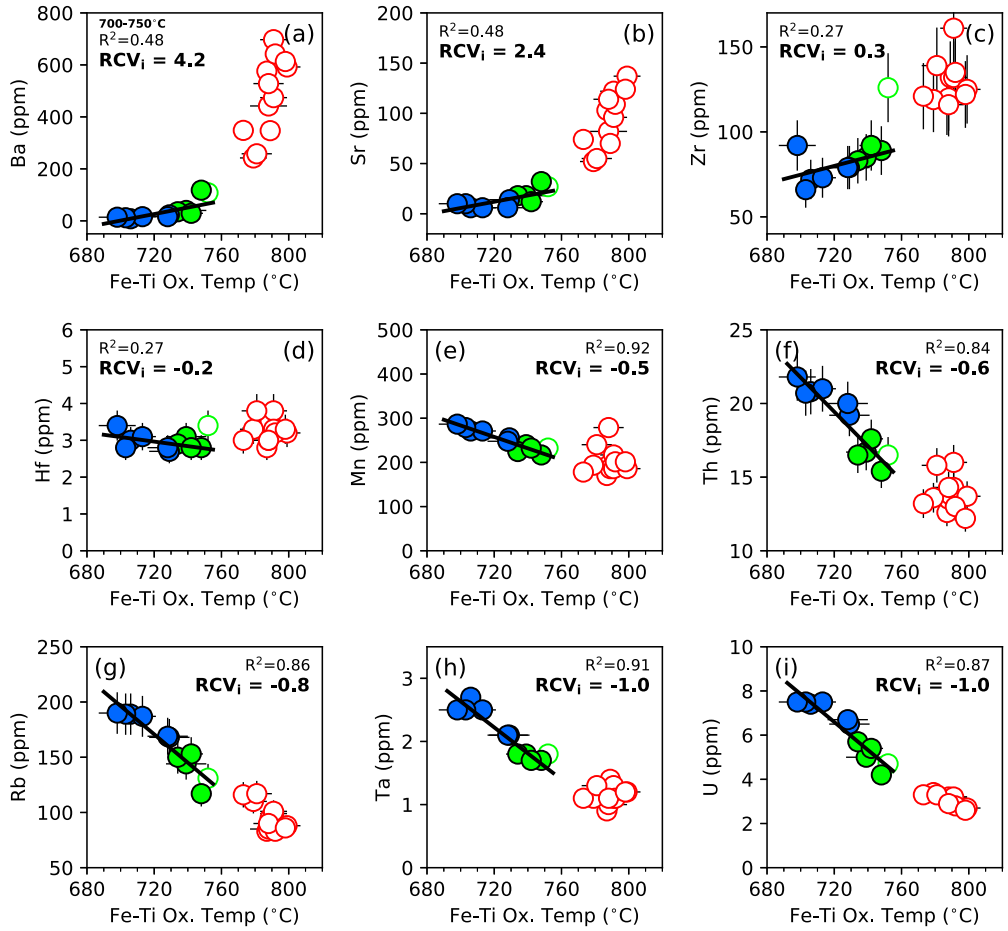

Fig. 7. Trace-element variations (ppm) with Fe–Ti oxide temperature (°C). Colors and symbols same as in Fig. 4.

compositions are provided in Supplementary Table 3, Supplementary Data, Electronic Appendix 1, and microprobe standards, detection crystals, and analytical error are reported in Supplementary Table 4, Supplementary Data, Electronic Appendix 1. The resulting partition coefficients for these six REE are listed in Table 3.

Biotite, titanomagnetite, and ilmenite

Mahood & Hildreth (1983) also reported trace-element partition coefficients for biotite (Bt), titanomagnetite (Mag), and ilmenite (Ilm) in Early-type Bishop samples from INAA (Table 3). For the major- and minor-element partition coefficients (e.g. Ti, Mg, Fe^{3+}, Fe^{2+}, Mn), the analyses from Jolles & Lange (2019) were used, and the results are shown in Table 3. For the partitioning of Fe^{3+} and Fe^{2+} between biotite and melt, it is assumed that the Fe^{3+}/Fe^{T} in biotite is the same as that in the melt.

Sanidine and plagioclase

Sanidine

Chamberlain *et al.* (2015) used laser ablation inductively coupled plasma mass spectrometry (LA-ICP-MS) to analyze trace-element concentrations in sanidine (Or_{65}) and glass in Early- and Transitional-type pumice clasts. These data were used to calculate partition coefficients for Ba, Sr, Eu, Ca, and Rb. As is commonly the case for constraints based on natural samples, there is a range of resulting D_i values, varying by nearly a factor of two for Ba and Sr. Therefore, to improve the accuracy and precision of estimated D_i values, the lattice strain model (e.g. Blundy & Wood, 1994; Wolff & Ramos, 2013) for sanidine was employed, which constrains the partitioning of different elements into a single lattice site on the basis of the radius of each element, and the elastic modulus of the lattice site (i.e. the ability to stretch or contract to accommodate element *i*). Onuma *et al.* (1968) observed that plots of logarithmic D_i versus ionic radius r_i for a range of elements show near-parabolic curves (Onuma diagrams), which can be described by the following strain model equation (Blundy & Wood, 1994):

$$\ln\left(\frac{D_i}{D_0}\right) = \frac{-4\pi EN_A\left[\frac{r_0\left(r_0-r_i\right)^2}{2} - \frac{\left(r_0-r_i\right)^3}{3}\right]}{RT} \qquad (2)$$

where D_i is the partition coefficient of an ion of radius r_i, D_i is the partition coefficient of an isovalent ion of radius r_0 that enters the lattice site without strain, E is the Young's modulus of the site, N_A is Avogadro's number, R is the universal gas constant and, T is absolute temperature. Following Wolff & Ramos (2013), in equation (2), E is estimated from

$$E \sim 1125Zd^{-3} \qquad (3)$$

Table 3: Element partition coefficients

Element	Quartz	Plagioclase*	K-spar*	Biotite†,‡	Titano-magnetite†,‡	Ilmenite†,‡	Allanite†	Zircon†	Apatite‡	RCV$_i$	Bulk D_i§
Ti				60·9	122	676	32·4			1·0	3·78
Fe^{3+}				32	282	56·9	20·5			0·3	1·90
Mg				117	3·6	9·38	13·4			0·4	1·93
Ca				0·12			18·8		83	0·3	2·17
Fe^{2+}		5·99	0·264	32	65·1	64·5	21·5			0·05	1·02
Ba		1·6	13	7						4·0	4·72
Sr		6·1	3·5							2·4	3·14
Rb		0·011	0·66	4·3						−0·8	0·28
Hf				0·65		0·65	28	3742		−0·2	0·94
Th				0·511	1·63	0·427	548	91·2		−0·6	0·55
U				0·131		0·063	17	383		−1·0	0·11
Mn				11	27·7	60·3	15·3			−0·5	0·51
Y									177	−1·3	0·04
La		0·3	0·048	3·4	11	1·31	2827	7·2	108	1·9	2·89
Ce		0·171	0·019	2·77	9·7	1·19	2494	10	163	1·5	2·52
Nd		0·075	0·005	2·2	6·9	0·96	1840	4·6	308	0·8	1·89
Sm		0·043	0·008	1·28	3·77	0·684	977	11·1	351	0	1·06
Eu		4·67	3	0·73	0·9	0·4	100	20		1·7	2·65
Dy				0·5		0·37	150	108	438	−0·9	0·29
Yb				0·32		0·55	37	564		−1·1	0·19
Lu				0·39		0·74	44	648		−1·0	0·22
Phase %§	∼32	∼34	∼31	1·60	0·42	0·34	0·093	0·024	0·025		

*Chamberlain *et al.* (2015).
†Mahood & Hildreth (1983).
‡This study.
§Phenocryst proportions based on P_{total} = 500 MPa and X_{H_2O} = 0·5.
Only elements used to constrain the stoichiometry of the crystallization/melting reaction with measured partition coefficients are presented here. RCV$_i$ of all elements analyzed and the predicted bulk partition coefficients and concentrations in the parental source for various melt fractions are given in Table 5.

Table 4: Compositions and temperatures of minimum liquidus and eutectic points

P (MPa)	X_{H_2O} fluid	Qz (wt%)	Kfs (wt%)	Ab (wt%)	*T* (°C)
200	1	36	25	39	680
200	0·7	35	29	36	701
200	0·5	35	31	34	750
350*	1	33·5	23·5	43	663
350*	0·7	33·5	28·5	38	656
350*	0·5	34	31·5	34·5	716
500	1	31	22	47	645
500	0·7	32	28	40	667
500	0·5†	33	32	35	682

Data from Holtz *et al.* (1992). Proportions of Qz + Kfs + Ab subsequently normalized to 97·5 % to account for 2·5 % abundance of other six mineral phases (see text).
*Interpolation.
†Extrapolation.

where Z is the ionic charge and d is the cation–oxygen distance (Blundy & Wood, 1994). Utilizing equation (2), the first step in this study was to start with the relatively well-known D_i values for the univalent ions, Na^+ and K^+, from Jolles & Lange (2019) for Or_{65} and then to obtain a best match to the parabola (Fig. 8) to constrain values for r_0 and D_0 (Fig. 8). In this study, the best match leads to a value for r_0 is 0.139 nm (close to the weighted average of 0.1395 nm for Na and K in Or_{65} sanidines from the Bishop Tuff), whereas D_0 is four. Extension to divalent ions (e.g. Ba, Sr, Eu^{2+}, Ca) was then made by utilizing the same r_0 as obtained for the univalent ions (0.139 nm), but adjusting D_0 (= 13) so that D_{Ca} (the best experimentally constrained partition coefficient among the divalent cations) is matched, within analytical uncertainty, by the parabola in Fig. 8. The results lead to improved constraints on the values for

D_{Ba} (= 13), D_{Sr} (= 3·5) and D_{Eu} (= 3) between sanidine (Or_{65}) and high-SiO_2 rhyolite melt. These values overlap the average (± 1σ) D_i values for these three elements, 14 (± 13), 2·0 (± 1·6) and 2·9 (± 1·8), respectively, from the analyses of Chamberlain *et al.* (2015).

Plagioclase

Chamberlain *et al.* (2015) also analyzed trace-element concentrations in plagioclase (An_{15}) in Early- and Transitional-type pumice clasts, allowing calculation of partition coefficients for key elements. Again, relatively large variations in D_i values were found, varying by nearly a factor of two for Ba and Sr. Fortunately, there are numerous experimental studies that report partitioning data for Ba and Sr between plagioclase and melts (Lagache & Dujon, 1987; Bindeman *et al.*, 1998; Bindeman & Davis 2000; Vander Auwera *et al.* 2000; Aigner-Torres *et al.* 2007; Tepley *et al.*, 2010; Dohmen & Blundy, 2014), including three experiments on relatively sodic plagioclase compositions (9–15 mol% An; Dohmen & Blundy, 2014).

As noted previously in the literature (e.g. Blundy & Wood, 1991), plagioclase composition exerts a first-order control on experimentally determined values of $RT\ln D_i$ (Fig. 9). There is far less scatter for $RT\ln D_{Ba}$ than for $RT\ln D_{Sr}$, and a linear fit between $RT\ln D_{Ba}$ and plagioclase composition closely recovers the experimental results on the relatively sodic plagioclases from Dohmen & Blundy (2014). For a composition of An_{15} and a temperature of 1000 K (727 °C), the linear fit gives a value for D_{Ba} of 2·1 (Fig. 9a). However, it is expected that the parental mush to the high-SiO_2 rhyolite portion of the Bishop Tuff may have contained a slightly more calcic plagioclase, closer to ~An_{20} (e.g. in Johnson leucogranite in Tuolumne Intrusive Suite; Bateman & Chappell, 1979), than what subsequently crystallized (~An_{15}) from the interstitial Bishop rhyolite after segregation. For An_{20} at 1000 K, the calculated value for D_{Ba} is 1·6, and is the best estimate of the value to apply to the parental mush (Table 3).

A similar evaluation is made for D_{Sr}, and although there is more scatter, there is also far more experimental data for $RT\ln D_{Sr}$ (Fig. 9b). A linear fit through all of the results recovers the experimental results on the three sodic plagioclase samples from Dohmen & Blundy (2014) equally well, which lends confidence that it provides the best estimate of D_{Sr} to apply in this study. At 1000 K and a plagioclase composition of An_{20}, the linear fit leads to a calculated value for D_{Sr} of 6·1, which is the value employed in Table 3.

CONSTRAINTS ON MINERAL–MELT REACTIONS IN THE PARENTAL MUSH

The primary question addressed in this study is whether the stoichiometry of the crystallizing/melting reaction in the parental mush, from which the interstitial melt was extracted (at different melt fractions) to form the high-SiO_2 rhyolite portion of the Bishop Tuff, can be constrained from the data summarized in Table 3. The following eutectic reaction is proposed:

$$\%X_1\mathrm{Qz} + \%X_2\mathrm{Pl} + \%X_3\mathrm{Kfs} + \%X_4\mathrm{Bt} + \%X_5\mathrm{Mag} + \%X_6\mathrm{Ilm} + \%X_7\mathrm{Zrn} + \%X_8\mathrm{Ap} + \%X_9\mathrm{Aln} = 100\,\%\,\mathrm{liquid}. \quad (4)$$

The goal is to constrain the values of X_1 to X_9 (relative proportion of each phase in the crystallizing/melting reaction) through an iterative set of linear fits to evaluate if a single, average stoichiometry can be obtained that leads to bulk partition coefficients for each element that are linearly correlated with their respective relative compatibility values. An additional constraint is that bulk $D_i = 1$ in the two cases where RCV_i is zero (i = Sm and Fe^{2+}). This will lead to bulk $D_i < 1$ for negative RCV_i and bulk $D_i > 1$ for positive RCV_i.

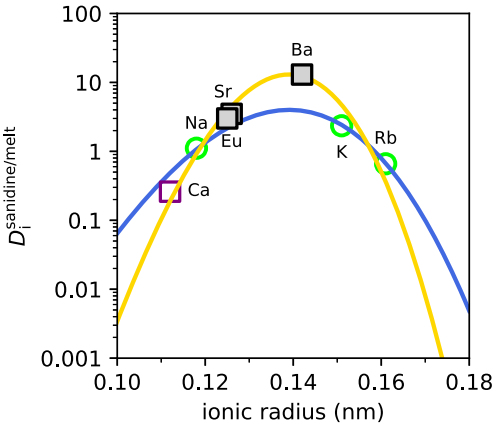

Fig. 8. Onuma diagram for element partitioning between sanidine and melt, where fitted curves are predictions from lattice strain theory [equation (2); see text]. Open symbols (green circle and purple square) denote literature values for univalent and divalent cations, respectively, from both Chamberlain *et al.* (2015) and Jolles & Lange (2019). Values for grey squares denote partition coefficients used, which overlap the values ±1σ from Chamberlain *et al.* (2015).

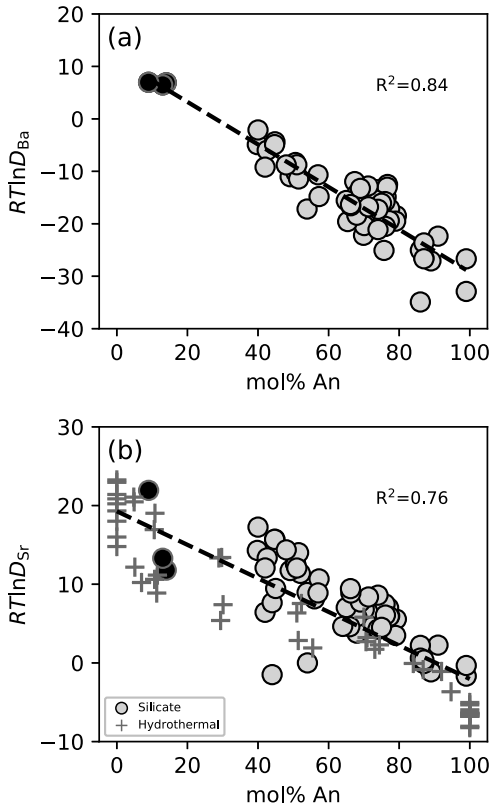

Fig. 9. Experimental plagioclase partition coefficients from literature for (a) Ba and (b) Sr against mol% anorthite. For Sr, experimental results for silicate melt (gray circles) and hydrothermal fluid (crosses) are both shown. Data for $RT\ln D_{Ba}$ follow a fairly tight linear trend, whereas there is more scatter for $RT\ln D_{Sr}$ results. Black circles denote relevant experiments for this study from Dohmen & Blundy (2014) (see text).

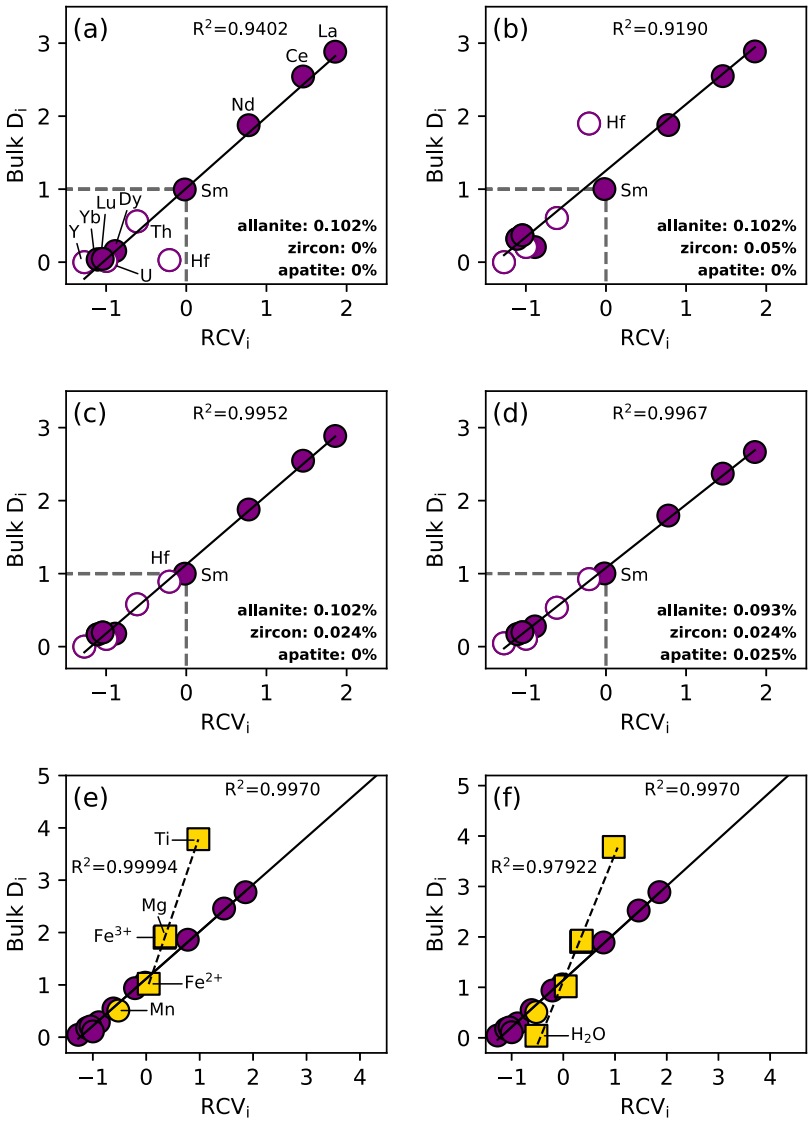

Fig. 10. (a–f) Plot of bulk D_i calculated from equation (5) and literature partition coefficients (Table 3) vs RCV$_i$ for each of 11 elements (filled symbols for REE and open symbols for Hf, Th, U, and Y). The bulk D_i for these 11 elements depend on only proportion of allanite, zircon, and apatite in crystallization/melting reaction (see text). In all cases, abundances lead to bulk $D_{Sm} = 1$ (RCV$_{Sm} = 0$). (a) Linear correlation between bulk D_i and RCV$_i$ for all REE, based only on allanite (see text). Only outliers are for elements (e.g. Hf and Y) that partition strongly into other phases (zircon and apatite, respectively; Table 3). (b) For illustration, the effect of adding 0·05 % zircon shows that Hf is an outlier in the opposite direction compared with (a). (c) Optimized abundance of zircon (0·024 %) that gives best fit to trace-element line (see text). (d) Optimized abundances of apatite (0·025 %), zircon (0·024 %), and allanite (0·093 %) that give best fit to trace-element line. (e) Minor-element line (dashed) and trace-element line (refitted based on recalculated bulk D_i using all six phases; see text). All trace elements now shown with filled symbols. Minor elements (yellow squares) follow a distinctly different trend from the trace elements (circles). It should be noted that Mn (yellow circle), a trace element in the Bishop Tuff, plots on the trace-element line obtained from allanite, zircon, and apatite, when its bulk D_i is calculated using the optimized abundances of the three ferromagnesian phases used to establish the minor-element line (see text). (f) Trace- and minor-element lines recalculated on the basis of added quartz, plagioclase, and K-feldspar proportions corresponding to 500 MPa and $X^{fluid}_{H_2O} = 0{\cdot}5$ (see Fig. 12 and text). H_2O is additionally incorporated on the minor-element line, where average D_{H_2O} (fluid–melt) = 4 and fluid abundance is 1 % (see text).

Evidence for a linear relationship between bulk D_i and RCV$_i$: constraints on % allanite, % zircon, and % apatite in reaction

The hypothesis evaluated in this study is that the RCV$_i$ for the trace elements are linearly correlated with their bulk partition coefficients (bulk D_i). An initial test of this hypothesis was made by examining the relationship between bulk D_i and RCV$_i$ for 11 trace elements (seven lanthanides, Y, Hf, Th, and U), which are entirely controlled by only three accessory phases: allanite, apatite, and zircon. Allanite is notable for its exceptionally large partition coefficients (~2830, ~2500, ~1840) for the light REE (LREE; La, Ce, Nd, respectively) that progressively decrease in magnitude (although remain large) for the middle REE (MREE) and heavy REE (HREE). Zircon predominantly controls the partitioning of Hf and U, and influences the HREE, whereas apatite is the only phase with a relatively high partition coefficient for Y (~180) and the MREE.

Ideally, the following model equation would be used for multiple linear regression:

$$\text{bulk } D_i = \left[D_i^{\text{Aln}} X_{\text{Aln}} + D_i^{\text{Zrn}} X_{\text{Zrn}} + D_i^{\text{Ap}} X_{\text{Ap}}\right]. \quad (5)$$

In equation (5), D_i^{Aln}, D_i^{Zrn}, and D_i^{Ap} are known parameters from the literature (Table 3), and X_{Aln}, X_{Zrn}, and X_{Ap} are the unknowns. The use of equation (5) in a multiple linear regression requires that the bulk D_i be known for each of the 11 trace elements, which is not the case. However, RCV_i are known for these 11 elements (Table 3), and if a linear relationship with bulk D_i values can be demonstrated, through a set of iterative steps (outlined below), it will allow bulk D_i values to be calculated and used in equation (5).

The first step in testing for a linear correlation between RCV_i and bulk D_i is to assign Sm a bulk D_i value of one because it has an RCV_i of approximately zero (Fig. 6). Next, an iterative approach was taken, where the proportions of zircon and apatite were first assumed to be zero, which allowed the proportion of allanite required to generate a bulk D_{Sm} of one to be calculated. For an allanite–liquid Sm partition coefficient of 977 (Table 3), the proportion of allanite is 1/977 (or 0·102 %). When these proportions (0·102 % allanite, 0 % zircon, 0 % apatite) were input into equation (5), the bulk D_i values for all 11 trace elements were calculated and plotted against their respective RCV_i. The results are shown in Fig. 10a and illustrate a remarkably strong linear correlation ($R^2 = 0{\cdot}940$). This is a notable result, as the RCV_i are obtained entirely from the Fe–Ti oxide thermometry results and whole-rock pumice clast analyses from Jolles & Lange (2019), whereas the bulk D_i values are based entirely on the Mahood & Hildreth (1983) partition coefficient results for allanite. This initial result strongly supports the hypothesis that RCV_i and bulk D_i values are linearly correlated.

The results in Fig. 10a show that the largest outlier from the linear trend is Hf, and the mineral–melt partition coefficient data in Table 3 show that this reflects the need to include zircon, owing to its large partition coefficient for Hf (~3742). For illustration, the addition of 0·05 % zircon is shown (Fig. 10b; no adjustment to % allanite is needed to ensure that bulk $D_{\text{Sm}} = 1$) to illustrate the effect on the calculated bulk D_i for Hf, which now deviates from the linear correlation with RCV_i in the opposite direction compared with the case of 0 % zircon, resulting in a lower R^2 (= 0·919). The optimal approach was to take iterative steps, and to add zircon to equation (5) in increments of 0·001 % (while adjusting the proportion of allanite each time to ensure that bulk $D_{\text{Sm}} = 1$) until the best linear fit between calculated D_i, using equation (5), and the RCV_i was found. The best fit ($R^2 = 0{\cdot}995$) occurs with 0·102 % allanite and 0·024 % zircon (Fig. 10c).

The final iterative step was to add apatite to equation (5), in increments of 0·001 % (and the proportion of allanite adjusted each time to ensure that bulk $D_{\text{Sm}} = 1$) until the best linear fit between bulk D_i and RCV_i was found (Fig. 10d). The final result ($R^2 = 0{\cdot}997$) leads to 0·093 % allanite, 0·024 % zircon, and 0·025 % apatite in the crystallization/melting reaction in equation (5). (See Supplementary Data, Electronic Appendix 3 for spreadsheets that perform these calculations.) The results allow the bulk partition coefficient for all 11 trace elements to be calculated (Table 3) and plotted as a function of their respective RCV values in Fig. 10d, which illustrates the strong linear correlation.

Effect of uncertainties in mineral–melt partition coefficients

Uncertainties in the mineral–melt partition coefficients for the 11 trace elements will affect the results in two different ways, depending on whether the errors are systematic or random. If there is a systematic error, and all D_i are too low (or too high) by a factor of two, then the deduced stoichiometry for the three mineral phases will also be too high (or too low) by a factor of two. If there are large, random errors among all D_i, moving them in different directions, then the R^2 values on the linear fits in Fig. 10 will degrade. The fact the R^2 values are >0·99 in Fig. 10c–d strongly supports the validity of the mineral–melt partition coefficients from the literature that were used (Table 3). In either case, the key conclusion that these three mineral phases (allanite, zircon, apatite) in the crystallization/melting reaction in the parental mush controlled the concentration gradients of these 11 trace elements with temperature remains robust.

Constraints on % biotite, % titanomagnetite, and % ilmenite in reaction

In the reaction in equation (4), only three phases control the bulk partition coefficients of Ti, Fe^{3+}, Fe^{2+}, Mg, and Mn: namely, biotite, titanomagnetite, and ilmenite. Therefore, the following model equation can be used to calculate the bulk D_i of these five elements:

$$\text{bulk } D_i = \left[D_i^{\text{Ilm}} X_{\text{Ilm}} + D_i^{\text{Mag}} X_{\text{Mag}} + D_i^{\text{Bt}} X_{\text{Bt}}\right]. \quad (6)$$

In equation (6), i refers to the following five elements: Ti, Fe^{3+}, Fe^{2+}, Mg, Mn.

Because the bulk D_i values for these five elements are not known, a test of a linear relationship with their respective RCV_i was performed. Once again, an iterative approach was taken, and first, an equal abundance of ilmenite and titanomagnetite was considered, without biotite. In this case, the initial abundances of the two Fe–Ti oxides were 0·75 % each, to generate a bulk $D_{\text{FeO}} = 1$ ($\text{RCV}_{\text{FeO}} = 0$). Biotite was then added in increments of 0·001 %, and the abundances of the two Fe–Ti oxides were adjusted (allowed to differ from each other) to ensure that bulk $D_{\text{FeO}} = 1$. It should be noted that an optimal linear fit between calculated bulk D_i, using equation (6) and RCV_i, could be obtained only when Mn (trace element) was not included. For the four minor elements (Ti, Fe^{3+}, Fe^{2+}, Mg), the best linear fit ($R^2 = 0{\cdot}9999$) is obtained with 1·60 % biotite, 0·42 % titanomagnetite, and 0·34 % ilmenite in the crystallization/melting reaction in equation (6). (See Supplementary Data, Electronic Appendix 3 for the spreadsheets that perform these calculations.)

Two different linear relationships between bulk D_i and RCV_i for trace- and minor-elements

When calculated bulk D_i values for Ti, Fe^{3+}, Fe^{2+}, and Mg (based on these three mineral proportions) are plotted as a function of their respective RCV_i in Fig. 10e, a strong linear correlation is shown, but with a distinctly different slope from that obtained for the trace elements. Interestingly, when these optimal proportions of biotite, titanomagnetite, and ilmenite are applied to calculate the bulk D_{Mn}, it plots on the line established for the 11 trace elements (obtained from mineral–melt partitioning involving allanite, zircon, and apatite) and not that for the four minor elements. This result strongly suggests that there is one linear relationship (between bulk D_i and RCV_i) for trace elements and another for minor elements. The reason for the two separate lines may reflect different partitioning behavior for trace vs minor elements (perhaps when Henrian behavior does or does not apply) in high-SiO_2 rhyolite melts.

One final step in the determination of bulk D_i values is to note that biotite, ilmenite, and titanomagnetite have non-zero partition coefficients for some of the actinide elements and REE, as well

as additional trace elements (e.g. Rb), which merits a new linear fit between all calculated bulk D_i and RCV_i, using the optimized proportions of all six phases (0·093 % allanite, 0·024 % zircon, 0·025 % apatite, 1·60 % biotite, 0·42 % titanomagnetite, and 0·34 % ilmenite). This updated linear fit for the trace elements is shown in Fig. 10e. This trace-element line allows the prediction of the bulk partition coefficients for Ba, Sr, Rb, and Eu; namely, those elements most strongly affected by the abundance of plagioclase and K-feldspar in the crystallization/melting reaction in equation (4). This will aid the determination of their proportions in the crystallization/melting reaction in the next subsection.

Effect of uncertainties in mineral–melt partition coefficients

Once again, uncertainties in the mineral–melt partition coefficients for the four minor elements will affect the results in two different ways, depending on whether the errors are systematic or random. If there is a systematic error, and all D_i are too low (or too high) by a factor of two, then the deduced stoichiometry of the three mineral phases will also be too high (or too low) by a factor of two. If there are large, random errors among all D_i, moving them in different directions, then the R^2 values on the linear fits in Fig. 10e will degrade. The fact the R^2 value is >0·99 in Fig. 10e strongly supports the validity of the mineral–melt partition coefficients from the literature that were used (Table 3). In either case, the main conclusion that these three mineral phases (biotite, titanomagnetite, ilmenite) in the parental mush controlled the concentration gradients of these four minor elements (Ti, Fe^{3+}, Fe^{2+}, Mg) and one trace element (Mn) with temperature remains robust.

Cause for increase in Fe^{3+}/Fe^{T} ($lnfO_2$ relative to Ni–NiO buffer) with temperature

The cause for the increase in Bishop Tuff oxidation state with temperature has long interested researchers (e.g. Hildreth, 1977; Carmichael, 1991; Ghiorso & Sack, 1991; Hildreth & Wilson, 2007; Ghiorso & Evans, 2008). Here, it is seen that the increase in Fe^{3+}/Fe^{T} with temperature in the high-SiO_2 rhyolite portion of the Bishop Tuff reflects the larger bulk partition coefficient for Fe^{3+} relative to that for Fe^{2+} during crystallization/melting in the parental mush, which in turn is caused by the fact that the proportion of the mineral phase (0·42 % titanomagnetite) in equation (4) with $D_{Fe^{3+}} > D_{Fe^{2+}}$ (282 > 65; Table 3) exceeds that of the phase (0·34 % ilmenite) with $D_{Fe^{3+}}$ slightly less than $D_{Fe^{2+}}$ (57 < 65; Table 3). In this study, it is assumed that $D_{Fe^{3+}} \sim D_{Fe^{2+}}$ for biotite (Table 3).

Constraints on % quartz, % plagioclase, % K-feldspar (location of eutectic)

The next objective was to constrain the relative proportions of quartz, plagioclase, and K-feldspar in the crystallizing/melting reaction in equation (4). This goal is equivalent to finding the location of the eutectic in the Qz–Pl–Kfs ternary, which is a strong function of pressure (P_{total}) and activity of water (Ebadi & Johannes, 1991; Holtz *et al*., 1992; Johannes & Holtz, 1996; Table 4) during crystallization/melting in the parental mush. Therefore, instead of beginning with the trace and minor elements that partition into plagioclase and K-feldspar (Ba, Sr, Rb, Eu, and Ca), published phase-equilibrium experimental results that document the location of the eutectic in the Qz–Pl–Kfs ternary under variable P_{total} and X_{H_2O} fluid compositions were initially employed. In Table 4, the proportion of each tectosilicate at the eutectic is summarized for three pressure conditions (200, 350, 500 MPa) and three X_{H_2O} fluid compositions (1, 0·7, 0·5) on the basis of the phase-equilibrium experiments from Holtz *et al*. (1992), which have been summarized by Johannes & Holtz (1996). It should be noted that the presence of the anorthite component in plagioclase has little effect on the location of the eutectic in the Qz–Pl(An–Ab)–Kfs system (Johannes, 1984; Johannes & Holtz, 1996).

With this information, bulk partition coefficients for Ba, Sr, Eu, and Rb were calculated for different P_{total}–X_{H_2O} fluid conditions, which translates to different tectosilicate proportions (Table 4), using the mineral–melt partition coefficient data for each element in Table 3. Because of the relatively large proportion of each tectosilicate phase (~25–35 % each) in the reaction in equation (4), the bulk D_i were recalculated for the 11 trace elements in Fig. 10e, incorporating the contributions from the tectosilicate phases (for each set of proportions in Table 4) as well as the ferromagnesian phases. A new linear fit to these 11 trace-elements was then obtained (not including Ba, Sr, Eu, and Rb, because an evaluation of their overlap with this revised linear fit is the test to be applied). When the various bulk D_i results (based on different tectosilicate proportions; Table 4) for Ba, Sr, Eu, and Rb are plotted as a function of their respective RCV_i (Fig. 11–c), a clear conclusion emerges. For calculated bulk D_i for these four trace elements to match those predicted by the updated trace-element line (Fig. 11), the X_{H_2O} must be <1. The best match between RCV_i and bulk D_i (for Ba, Eu, and Rb) is obtained for an average X_{H_2O} fluid composition of ~0·5 at pressures of 500 and 350 MPa (Fig. 11). Therefore, the results lead to average proportions of the tectosilicate phases in the reaction in equation (4) of ~32–33 % quartz, ~34 % plagioclase, and ~31 % K-feldspar.

Effect of uncertainties in mineral–melt partition coefficients

In the case of the tectosilicates, the mineral–melt partition coefficients for Ba and Sr most strongly affect the inferred stoichiometry of K-feldspar and plagioclase, respectively, in the crystallization/melting reaction. Thus, if the D_i for both Ba and Sr increase (or decrease), the deduced proportions of K-feldspar and plagioclase in the reaction will both decrease (or increase), which will lead to a higher (or lower) inferred proportion of quartz in the reaction. If the D_i values for Ba and Sr are changed in different directions, then the K-feldspar and plagioclase proportions will change accordingly. The most important point is that if the D_i values for these two elements change by more than 15 % from the values in Table 3, then the deduced proportions of K-feldspar, plagioclase and quartz in the crystallization/melting reaction do not match any eutectic composition in the Qz–Pl–Kfs–H_2O system. The fact that the best estimates of the D_i values for Ba and Sr from the literature (Table 3), based on the employment of a lattice strain model (Fig. 8) and experimental partitioning data (Fig. 9), lead to geologically reasonable results (i.e. melt segregation depths of ~350–500 MPa, $X_{H_2O} \sim 0{\cdot}5$), underscores the robustness of the approach and the data employed.

CONSTRAINTS ON FLUID–MELT REACTIONS IN THE PARENTAL MUSH

The optimal linear fits in Fig. 11 indicate an average X_{H_2O} fluid composition of ~0·5 and a total pressure of ~350–500 MPa during the crystallization/melting reaction in the parental mush. These two constraints can be combined with analyzed volatiles in quartz-hosted melt inclusions from the Bishop Tuff, which were trapped during phenocryst growth at ~100–200 MPa (Wallace *et al*., 1999; Anderson *et al*., 2000; Roberge *et al*., 2013; Myers *et al*., 2019), to

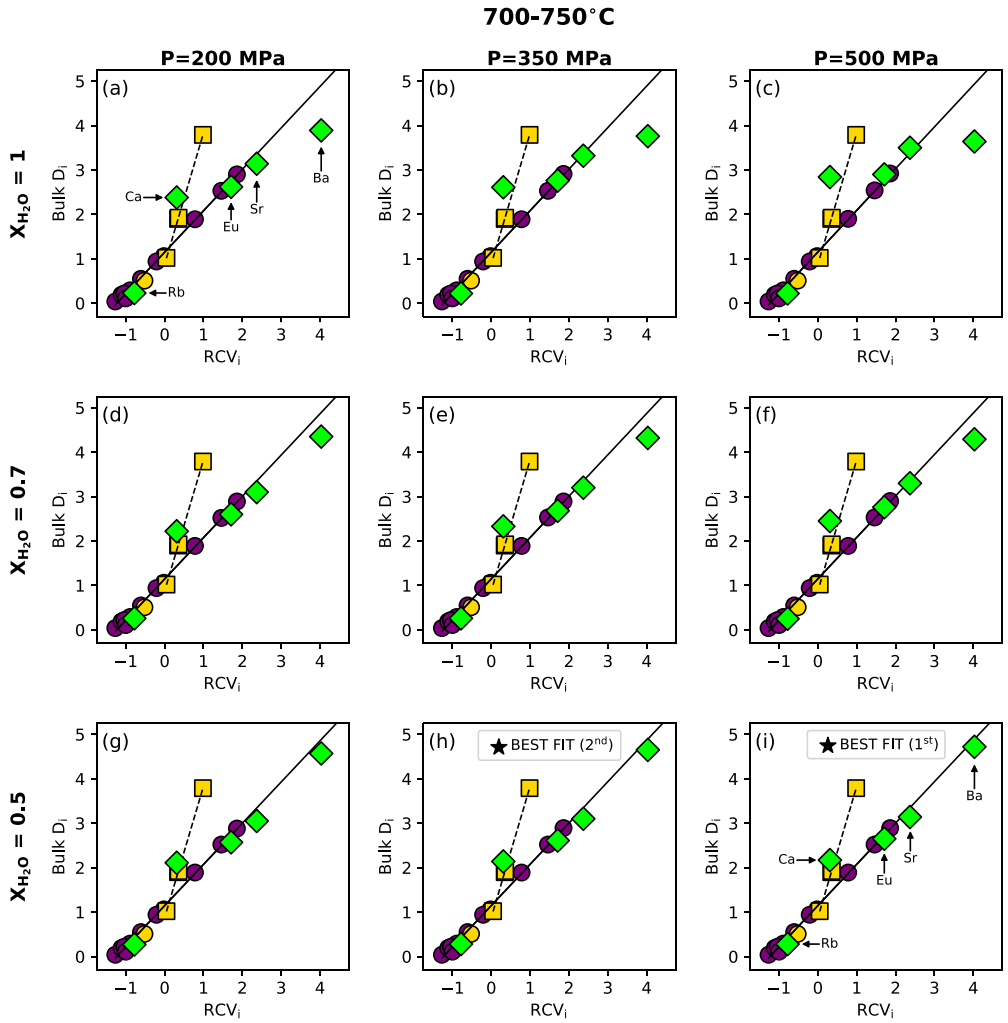

Fig. 11. Bulk D_i vs RCV_i from Early- and Transitional-type Bishop Tuff samples for various locations of eutectic (Table 4; various P_{total} and $X_{H_2O}^{fluid}$). Colors and symbols same as in Fig. 10, with addition of green diamonds for Ba, Sr, Eu, Rb (elements affected by feldspar proportions; Table 4). Black stars on subplots denote best fits to predicted bulk D_i given P_{total} and $X_{H_2O}^{fluid}$ values.

evaluate degassing paths after segregation of interstitial melts from the parental mush.

The concentrations of H_2O and CO_2 in high-SiO_2 rhyolite during fluid-saturated ascent, following open- and closed-system degassing paths, were calculated for various initial fluid compositions at 350 MPa and 500 MPa, respectively (Fig. 12), using VolatileCalc2 (Newman & Lowenstern, 2002). A temperature of 750 °C was used in these calculations because allanite is required to be present in the parental mush, which constraints temperatures to be <770–780 °C (Vazquez *et al.*, 2004). It is expected that the actual degassing paths were between these two endmembers (open- and closed-system). Importantly, closed-system degassing paths vary as a function of the initial % fluid present at the time of melt segregation, which provides an upper-limit constraint on fluid abundance.

The results in Fig. 12 show that segregation at 350 MPa requires a more H_2O-rich fluid phase ($X_{H_2O}^{fluid}$ ~ 0·7–0·5) to overlap with Early- and Transitional-type MI volatile analyses (Wallace *et al.*, 1999; Anderson *et al.*, 2000; Roberge *et al.*, 2013; Myers *et al.*, 2019), whereas at 500 MPa, the optimal range in fluid composition is $X_{H_2O}^{fluid}$ ~ 0·6–0·4. Therefore, an average depth of 500 MPa (rather than 350 MPa) more closely fits the evidence of an average fluid composition of X_{H_2O} ~ 0·5 during melt segregation, which is consistent with results from Fig. 11. Importantly, a range in melt segregation depths is not precluded (e.g. 550–400 MPa or ~21–15 km), nor a range in fluid composition (e.g. $X_{H_2O}^{fluid}$ ~ 0·6–0·4).

Results are also shown for MI data from quartz cores in Late-type Bishop samples, which grew from a high-SiO_2 rhyolite endmember prior to mixing (Roberge *et al.*, 2013). If the high-SiO_2 rhyolite endmember, which mixed with a less differentiated melt to form the Late-type rhyolite, segregated from the same (or similar) granitoid mush at ~500 MPa, but at higher melt fractions (i.e. higher temperatures), the fluid composition must have been $X_{H_2O}^{fluid}$ ~ 0·4–0·3.

An additional conclusion derived from the degassing paths (Fig. 12) is that the greatest overlap with the MI data is found for fluid mass abundances during melt segregation that are predominantly ≤1 wt%. Corroboration of this low fluid abundance is provided by the incompatible behavior of H_2O (Fig. 3a) and the compatible behavior of CO_2. Utilizing VolatileCalc2 and a fluid composition of $X_{H_2O}^{fluid}$ = 0·5 (± 0·1) at 500 MPa, the calculated D_{H_2O} and D_{CO_2} (fluid–melt) values are ~4 (± 0·5) and ~312 (± 24),

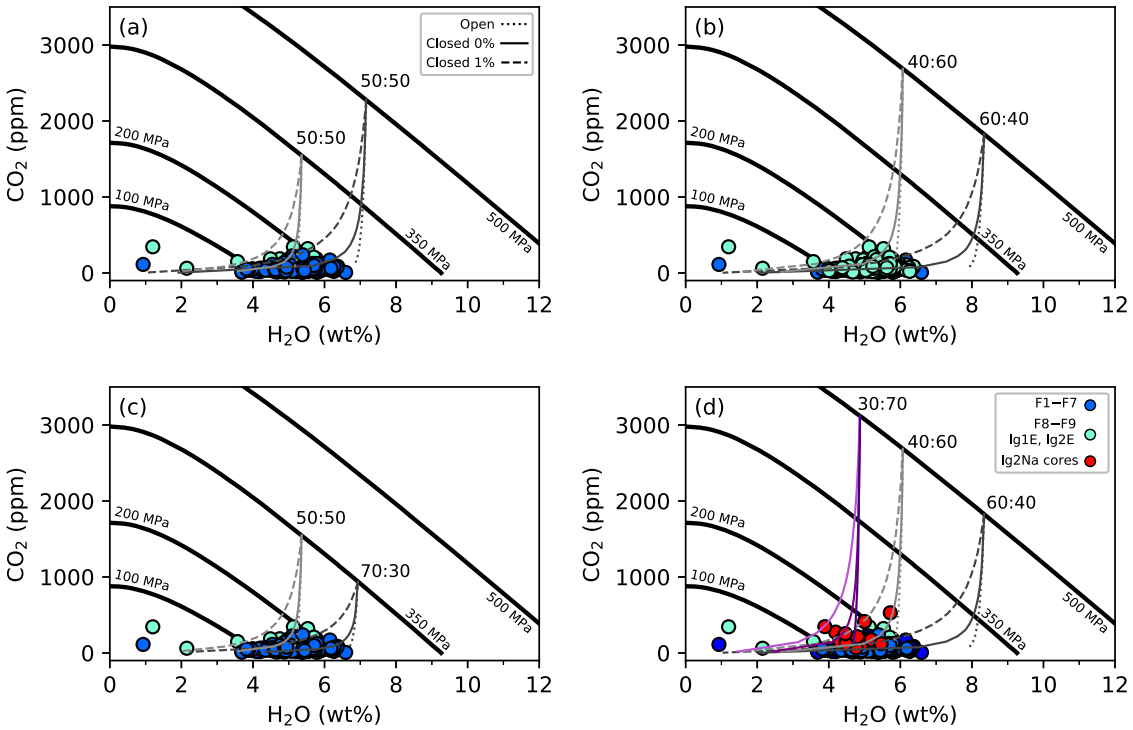

Fig. 12. CO_2 (ppm) vs H_2O (wt%) degassing paths (both open and closed system; Volatile Calc2, Newman & Lowenstern, 2002) initiated at different pressures (500 and 350 MPa) and fluid compositions (X_{H_2O} and X_{CO_2})—conditions at onset of melt segregation—that lead to overlap with volatile analyses in quartz-hosted melt inclusions (MIs) from the literature (Wallace *et al.*, 1999; Anderson *et al.*, 2000; Roberge *et al.*, 2013; Myers *et al.*, 2019). Thick, black lines are isobars for 500, 350, 200, and 100 MPa. Blue symbols denote Early-type airfall (F1–F7) units, whereas aqua samples—those from units F8 and F9, Ig1E, and Ig2E—could be either Early- or Transitional-type (unable to distinguish). (a) Two degassing paths, with same initial $X^{fluid}_{H_2O}$ composition (0·5), but different segregation pressures (350 and 500 MPa). (b) Two degassing paths at the same pressure but different initial $X^{fluid}_{H_2O}$ (0·4 and 0·6). Aqua samples plotted on top of blue samples to highlight distribution of aqua samples. (c) Two degassing paths at same segregation pressure (350 MPa) but different $X^{fluid}_{H_2O}$ (0·5 and 0·7). (d) Same as (b) except for the addition of volatile analyses from MIs in cores of quartz (crystallized from high-SiO_2 rhyolite endmember) in Late-type pumice (red circles; Roberge *et al.*, 2013), and a third degassing path with lower $X^{fluid}_{H_2O}$ (0·3) that overlaps the lower H_2O and higher CO_2 concentrations analyzed in the MIs in quartz cores from Late-type samples.

respectively, which reflect the much higher solubility of H_2O relative to CO_2 in the melt at these P–T conditions (500 MPa; 750 °C). For a fluid abundance of ~1 %, the bulk D_{H_2O} is ~0·04 and bulk D_{CO_2} is ~3·1, which is consistent with the respective incompatible and compatible behavior of H_2O and CO_2 during the crystallization/melting reaction in the parental mush. Moreover, the very low bulk D_{H_2O} value (~0·04) is consistent with the RCV_i for H_2O of −0·51, based on a revised fit to the minor-element linear relationship (Fig. 10f) that uses the tectosilicate abundances at 500 MPa and an average fluid composition of X_{H_2O} = ~0·5.

SOURCE OF VOLATILES IN BISHOP TUFF RHYOLITE: THE ROLE OF BASALTS

Thus far, the hypothesis that the geochemical gradients with temperature in the high-SiO_2 rhyolite portion of the Bishop Tuff (i.e. not those owing to magma mixing) were caused by segregation of variable fractions of interstitial melt in a parental mush has been demonstrated to be viable, under the condition that it occurred at an average depth and temperature of ~500 MPa and ~750 °C, respectively, where nine mineral phases were present, including allanite, as well as a small amount of excess fluid (≤1 wt%) with an average composition of X_{H_2O} ~ 0·5. Under these conditions, the calculated solubility of H_2O and CO_2 is ~7·2 wt% and ~2269 ppm, respectively (using VolatileCalc2). The next question to address, therefore, is the source of this substantial concentration of volatiles in the granitoid mush.

Irrespective of whether the interstitial melt formed by crystallization (from an initial 100 % melt that contained dissolved volatiles) or partial melting (of sub-solidus granitoid in the presence of a fluid phase), the primary source of the volatiles must have been from basaltic sills or dikes emplaced into the crust beneath Long Valley caldera, as the pre-existing granitoid crust beneath Long Valley caldera contains only a small amount of water (<0·6 wt%) in the form of ≤10 modal % biotite/hornblende (Bateman & Chappell, 1979). The material involvement of the Long Valley basalts in the origin of the Long Valley rhyolites, including the Bishop Tuff, has long been established (e.g. Halliday *et al.*, 1984; Davies *et al.*, 1994; Simon *et al.*, 2014). In a recent study, Calogero *et al.* (2020) presented a numerical model of the thermal evolution of the crustal column beneath Long Valley caldera owing to the injection of basaltic sills. A central conclusion from that study is that the Long Valley basalts were a source not only of heat (and mass), but also of volatiles, and both were required to drive rhyolitic volcanism at Long Valley.

In a recent study, Jolles & Lange (2021) constrained the average water contents (~4 wt%) of the Plio-Quaternary Long Valley basalts, which erupted in close association with the Long Valley caldera (e.g. Cousens, 1996). An estimate of CO_2 contents in these basalts, based on comparison with similar basalts, is ~2000–6000 ppm CO_2 (e.g. Wallace, 2005). Here, we present a mass-balance calculation of the

minimum mass of basalt required, if all of the water in the interstitial rhyolite melt in the parental source was primarily derived from the basalts. The high-SiO_2 rhyolite portion of the Bishop Tuff (Early- and Transitional-type) is estimated to be ≥400 km^3 (Hildreth & Wilson, 2007), which converts to ~8·8 × 10^{14} kg of rhyolite melt (density of 2200 kg m^{-3} at 500 MPa; Lange & Carmichael, 1987; Lange, 1997; Ochs & Lange, 1999; Guo *et al.*, 2014). For an average dissolved water content of ~7·2 wt% in the interstitial melt, this translates to ~6·3 × 10^{13} kg of H_2O. The amount of basalt that contains this much water is ~630 km^3, if it contains ~4 wt% H_2O and thus has a melt density of ~2500 kg m^{-3} at 500 MPa. However, if the water from the basalt is derived by degassing after complete crystallization, then the amount of water available for transfer to the rhyolites may only have been ~3 wt%, as ≤1 wt% may have been held in hydrous mineral phases (based on modal abundances of biotite/hornblende in an average basaltic amphibolite; Sisson *et al.*, 2005). In this case, the needed volume of basalt is ~840 km^3. It should be noted also that the composition of the fully degassed fluid phase [~3 wt% H_2O + 4000 (± 2000) ppm CO_2] is $X^{fluid}_{H_2O}$ = 0·95 (± 0·02). If pre-existing granitoid crust also makes a small contribution to the water budget of the parental body, then the required volume of basalt is <840 km^3.

Origin of volatile concentration gradients in the interstitial melt

There are different mechanisms and timescales that are possible for the transfer of water from the basalts, and a detailed examination of those processes is beyond the scope of this study. Here, the goal is to understand how the transfer of a fluid phase (initially from basalts) to the interstitial melt in the parental mush could lead to the observed gradients in the H_2O and CO_2 concentrations with melt fraction (temperature). Two endmember cases are considered: (1) crystallization of an initial 100 % melt that already contains dissolved H_2O and CO_2; (2) partial melting of an initially sub-solidus leucogranite in the presence of an H_2O-rich fluid phase.

The first scenario requires the parental liquid to have a volume >1200 km^3 (if ~35 % interstitial melt constitutes a volume of ~400 km^3). This scenario may be an oversimplification as there is growing consensus that such a large reservoir of fully molten melt is unlikely. But if it did exist, it must have started with ~2·52 wt% H_2O so that after 65 % crystallization there was ~7·2 wt% H_2O dissolved in the interstitial melt. The concentration of CO_2 must have been ≤3879 ppm; the upper bound is based on fluid-saturation conditions at 500 MPa for a melt with 2·52 wt% H_2O dissolved in the melt. These are the initial conditions required for closed-system, isobaric crystallization at 500 MPa to form a 35 % interstitial melt fraction, which contained ~7·2 wt% H_2O and ~2269 ppm CO_2.

In the second scenario, the interstitial high-SiO_2 rhyolite melt is formed by partial melting of a leucogranite (containing the same nine mineral phases as seen in the high-SiO_2 rhyolite portion of Bishop Tuff) in the presence of a fluid derived from the basalts ($X^{fluid}_{H_2O}$ ~ 0·95). The presence of such an H_2O-rich fluid strongly lowers the solidus temperature of granitoids. For example, melt fractions of ~35 % are fully expected at ~750 °C and 500 MPa, as seen in plots of melt fraction vs temperature curves for granitoid from Calogero *et al.* (2020), which are based on rhyolite-MELTS calculations (Gualda *et al.*, 2012).

For the case of a fixed mass of H_2O-rich fluid present at the onset of partial melting of a granitoid, it is expected that the H_2O and CO_2 concentrations in both the interstitial melt and the fluid phase will change (co-evolve) as melt fraction increases, which is illustrated in Fig. 13. At the granitoid solidus, the initial fluid composition (exsolved from crystallized basaltic sills) is $X^{fluid}_{H_2O}$ ~ 0·95. After an interstitial melt forms, the fluid phase (with a finite mass) progressively dissolves into an increasing mass of melt (as melt fraction increases; Fig. 13). As melt fraction increases, a disproportionate amount of H_2O vs CO_2 in the fluid partitions into the melt, owing to the much higher solubility of H_2O relative to CO_2 in rhyolite melt (and thus significantly different partition coefficients of ~4 vs ~312 respectively at these P–T conditions), which in turn drives the fluid composition to lower $X^{fluid}_{H_2O}$ values (Fig. 13a). The evolving H_2O and CO_2 contents in the interstitial melt, as melt fraction increases, are shown in Fig. 13b and c. Melts formed at lower melt fractions (i.e. lower temperatures), namely the Early-type rhyolites, are relatively H_2O-rich and CO_2-poor, with a fluid composition of $X^{fluid}_{H_2O}$ ~ 0·6–0·5 at the time of melt segregation, whereas those melts formed at progressively higher melt fractions (i.e. higher temperatures) namely Transitional-type rhyolites, contain less H_2O and more CO_2, with a fluid composition of $X^{fluid}_{H_2O}$ ~ 0·5–0·4 during melt segregation. Finally, in the case where melt fractions increase further, and the fluid composition ranges to $X^{fluid}_{H_2O}$ ~ 0·4–0·3, the resulting melts are plausible candidates for the high-SiO_2 rhyolite endmember to the Late-type Bishop rhyolites, which mixed with less differentiated melts prior to eruption. Thus, progressive partial melting of granitoid, which has interacted with a finite mass of H_2O-rich fluid from degassed basalts, is expected to produce an evolving fluid composition as well as an evolving interstitial melt composition (Fig. 13) in terms of their respective H_2O and CO_2 concentrations.

BREAK IN GRADIENT SLOPES BETWEEN EARLY- AND TRANSITIONAL-TYPE SAMPLES: CHANGE IN STOICHIOMETRY OF CRYSTALLIZATION/MELTING REACTION?

A close examination of element concentration plots with temperature shows that there is a consistent break in slope between Early- and Transitional-type samples. Previously, the deduced stoichiometry of the mineral–melt reaction in equation (4) was derived from both Early- and Transitional-type samples, and it is thus an average for melts extracted over a range of temperature (700–750 °C). Here, the Early- and Transitional-type samples are evaluated separately to deduce a possible difference in the stoichiometry of the crystallization/melting reaction in the granitoid mush at lower (Early-type) versus higher (Transitional-type) temperatures (melt fractions).

In Fig. 14, concentration plots with temperature are shown for a subset of representative elements (plots for all elements can be found in Supplementary Fig. 1, Supplementary Data, Electronic Appendix 4), where slopes are obtained over two distinct temperature intervals: 700–730 °C and 725–750 °C. From these plots, a revised set of RCV_i were obtained for all minor and trace elements, based only on samples between 725 and 750 °C (predominantly Transitional-type). The stoichiometry of the reaction in equation (4), utilizing these revised RCV_i (725–750 °C; Table 5), was then constrained using the same procedures that were followed for the entire dataset (700–750 °C) above. The details are provided in Supplementary Data, Electronic Appendix 5, but the key findings are summarized here.

For the three accessory phases, which control the behavior of numerous trace elements, the optimal fit (R^2 = 0·993) to equation (5) leads to 0·095 % allanite, 0·03 % zircon, and 0·02 % apatite. This

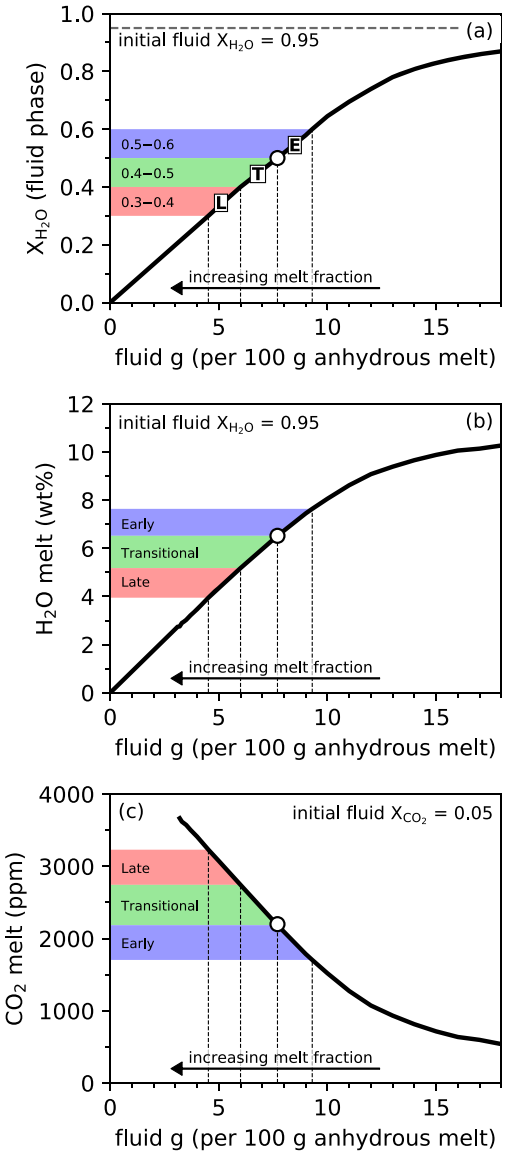

Fig. 13. Change in $X^{fluid}_{H_2O}$ composition with decreasing abundance of initial fluid (derived from degassing of Long Valley basalts; see text) relative to mass of interstitial melt owing to increasing melt fraction (with increasing temperature). (a) For a fixed abundance of initial fluid ($X^{fluid}_{H_2O} \sim 0{\cdot}95$), as the mass of interstitial melt increases with melt fraction, more H_2O dissolves in the melt relative to CO_2 (owing to different fluid–melt partition coefficients), which depletes H_2O in the fluid phase. Highlighted are $X^{fluid}_{H_2O}$ compositions during initial segregation of Early- (E), Transitional- (T), and Late-type (L) Bishop magma (high-SiO_2 rhyolite endmember), which lead to degassing paths that match MI analyses (Fig. 12), and the corresponding amount of initial fluid required. White circle denotes $X^{fluid}_{H_2O}$ = 0·5. (b) Concentrations of H_2O (wt%) dissolved in interstitial high-SiO_2 rhyolite for various $X^{fluid}_{H_2O}$ compositions shown in (a). (c) Same as (b), but for CO_2 (ppm). It should be noted that with increasing melt fraction, the concentration of H_2O and CO_2 in the melt decreases and increases, respectively, consistent with incompatible vs compatible behavior, respectively (see text).

result is only slightly different from that obtained for the entire 700–750 °C dataset, with slightly more allanite and zircon, and a little less apatite. For the three ferromagnesian phases, which control the behavior of Ti, Fe^{3+}, Fe^{2+}, Mg (and Mn), the best fit (R^2 = 0·997) to equation (6) is 1·88 % biotite, 0·18 % titanomagnetite, and 0·44 % ilmenite. Again, the results are broadly similar, with slightly more biotite, slightly less titanomagnetite, and slightly more ilmenite.

For the tectosilicate phases, the best fit for Ba, Sr, Eu, and Rb on the trace-element line is again for an average location of the eutectic at 500 MPa, but points to $X^{fluid}_{H_2O}$ that is slightly lower than 0·5 (the average value inferred for the entire 700–750 °C data set). This result is fully consistent with a progressively lower $X^{fluid}_{H_2O}$ with increasing temperature (i.e. melt fraction) in the parental crystal-rich mush (Figs 12 and 13).

A similar exercise can be applied to the Early-type only dataset, although the relative errors in the RCV_i are larger owing to the flatter (smaller-magnitude) slopes. The details are provided in Supplementary Data, Electronic Appendix 6, but the key findings are summarized here. The optimal proportions of the three accessory phases are 0·089 % allanite, 0·004 % zircon, and 0·039 % apatite, whereas those for the three ferromagnesian phases are 0 % biotite, 1·14 % titanomagnetite, and 0·40 % ilmenite. These two combined results suggest that zircon and biotite did not participate in the crystallization/melting reaction at these lower temperatures. Although this outcome may be an artifact of the larger errors in RCV_i, it probably reflects the fact that these two phases are known to be fairly refractory relative to hydrous, low-temperature, eutectic melting in the Qz–Pl–Kfs system (e.g. Piwinskii & Wyllie, 1968; Hanchar & Watson, 2003). Thus, it does not preclude the presence of these two phases, only that they were not participating in the crystallization/melting reaction. For the tectosilicates, no match could be found to any of the eutectic conditions in Table 4 (P_{total} = 200–500 MPa; X_{H_2O} = 1·0–0·5), which points to wholesale segregation of late-stage (i.e. close to 'true eutectic') interstitial melt during crystallization. In exposed granitoid plutons, similar late-stage, 'eutectic-like' melts are found in thin aplite dikes, which rarely escape their host plutons (Glazner *et al.*, 2008, 2020). Alternatively, the results could reflect nearly complete 100 % melting (i.e. 'true eutectic' behavior) of the first melts to form and segregate. The essential point is that the Early-type samples have bulk compositions that are close to those of aplite dikes and overlap 'true eutectic' melts at the P–T–X_{H_2O} conditions deduced for the parental mush to the high-SiO_2 rhyolite portion of the Bishop Tuff. How these late-stage melts efficiently segregated, when aplite dikes fail to do so at the time of their initial formation, will be addressed in future work. The key point is that the geochemical evidence strongly points to their 'true eutectic' character at the time of their segregation.

CONSTRAINTS ON THE BULK COMPOSITION OF THE PARENTAL MUSH TO THE HIGH-SiO_2 RHYOLITE PORTION OF THE BISHOP TUFF

One of the key results from this study is the determination of the average bulk partition coefficient for each element (bulk D_i; Table 3) between the crystal-rich portion of the parental mush and the interstitial melt, where the latter segregated over a range of melt fractions to form the high-SiO_2 rhyolite portion of the Bishop Tuff. These bulk D_i values allow the average bulk composition of the parental mush (C_i^{parent}) to be constrained using equation (1). For this calculation, the concentration of each element in the interstitial melt (C_i^{liquid}) is taken as the average of all Early- and Transitional-type high-SiO_2 rhyolite samples (Table 5). To calculate C_i^{parent}, a range of melt fraction (F) values were employed (0·2, 0·35, 0·5).

The results are presented in Table 5 and show that the average minor-element composition of the parental source to the high-SiO_2

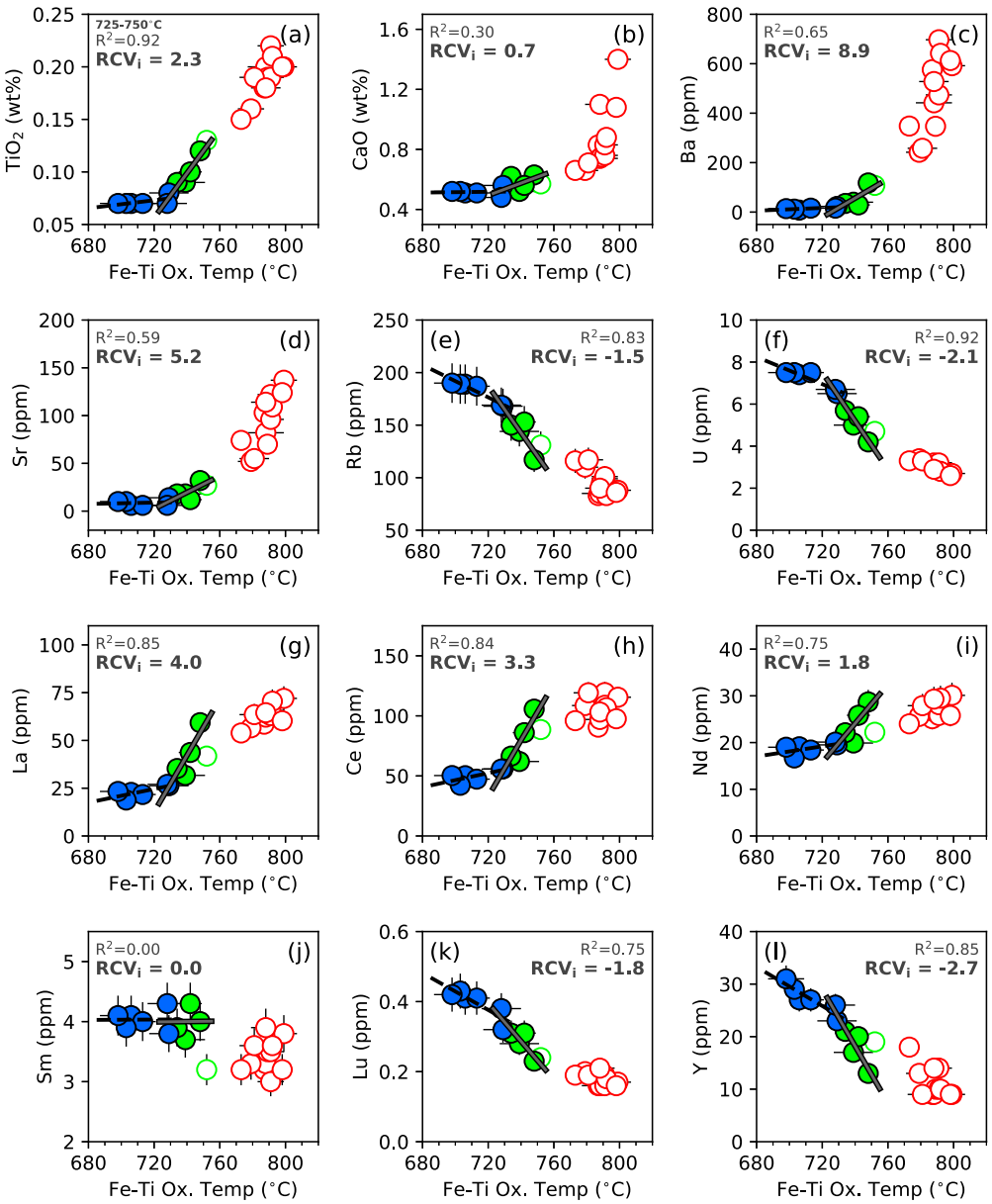

Fig. 14. Select plots of concentration (wt% and ppm) vs Fe–Ti oxide temperature (°C) for Bishop pumices, illustrating the break in slope for data between 700–730 °C and 725–750 °C. New RCV_i are calculated for the 725–750 °C group of samples, and their slopes are designated with a grey line. Also shown is the slope of concentration vs temperature for the 700–730 °C samples, designated with a dashed black line. Similar plots for all elements are provided in Supplementary Fig. 1, Supplementary Data, Electronic Appendix 4. Error bars represent 2σ uncertainty (see text).

rhyolite portion of the Bishop Tuff (i.e. Early- and Transitional-type), for an average melt fraction of 35 (± 15) %, was ~0·23 (± 0·04) wt% TiO_2, ~0·87 (± 0·02) wt% FeO^T, ~0·15 (± 0·01) wt% MgO, ~0·96 (± 0·10) wt% CaO, and an average Fe^{3+}/Fe^T of ~0·33 (± 0·02). In terms of trace-element composition, it is estimated to have contained ~106 (± 17) ppm Ba, ~32 (± 4) ppm Sr, ~88 (± 18) ppm Rb, ~69 (± 9) ppm La, ~124 (± 14) ppm Ce, ~33 (± 3) ppm Nd, and ~9 (± 3) ppm Y. Estimates for all other trace-element average compositions are listed in Table 5.

A major take-away is that the parent to the high-SiO_2 rhyolite portion of the Bishop Tuff was itself significantly differentiated, with relatively low Ba (≤123 ppm) and Sr (≤36 ppm), and yet it was notably enriched in La (≤78 ppm) and Ce (≤138 ppm) compared with most Mesozoic granitoids in the Sierra Nevada batholith, including leucogranites. For example, the Johnson Granite Porphyry is the most differentiated part of the Tuolumne Intrusive Suite and yet it contains 92–484 ppm Sr and 325–1170 ppm Ba, along with ≤33 ppm La and ≤61 ppm Ce (e.g. Bateman & Chappell, 1979; Coleman *et al.*, 2012). The elevated La and Ce contents in the parent to the high-SiO_2 rhyolite portion of the Bishop Tuff point to an origin that included material contributions from the Plio-Quaternary Long Valley basalts, which have elevated concentrations of the LREE (Cousens, 1996). This conclusion is consistent with isotopic data from the literature (e.g. Halliday *et al.*, 1984; Simon *et al.*, 2014) that also demonstrate the material involvement of the Long Valley basalts, as well as pre-existing granitoid crust, in the origin of the parental mush to the

Table 5: *Average composition, RCV*$_i$*, bulk* D$_i$ *and predicted composition of parent source for various melt fractions*

Element	700–750 °C						725–750 °C		
	Av. C_i	RCV$_i$	Bulk D_i*	C_0 (F = 0·2)	C_0 (F = 0·35)	C_0 (F = 0·5)	Av. C_i	RCV$_i$	Bulk D_i*
TiO_2	0·08	0·98	3·78	0·27	0·23	0·20	0·09	2·31	4·33
FeO	0·60	0·05	1·02	0·61	0·61	0·61	0·61	0·34	1·02
Fe_2O_3	0·18	0·34	1·90	0·31	0·29	0·27	0·19	0·52	1·38
MgO	0·10	0·36	1·93	0·17	0·15	0·14	0·10	1·15	2·25
CaO	0·54	0·31	2·17	1·05	0·96	0·86	0·56	0·72	2·16
Ba	31	4·03	4·72	124	106	89	44	8·92	4·73
Sr	13	2·37	3·14	36	32	27	17	5·17	3·14
Rb	166	−0·78	0·28	70	88	106	150	−1·48	0·29
Zr	81	0·32	1·43†	109	104	99	85	0·73	1·40
Nb	14	−0·82	0·37†	7	8	10	13	−1·45	0·45†
Cs	4·9	−1·1	0·10†	1·4	2·0	2·7	4·2	−2·30	0·08†
Th	19·0	−0·61	0·55	12·1	13·4	14·7	17·6	−1·07	0·56
Hf	2·9	−0·21	0·94	2·8	2·8	2·9	2·9	0·14	1·16
Ta	2·1	−0·96	0·23†	0·8	1·1	1·3	1·9	−1·16	0·58†
U	6·3	−1·00	0·11	1·8	2·7	3·5	5·6	−2·07	0·13
Mn	252	−0·52	0·51	153	171	190	235	−0·66	0·53
Y	23	−1·27	0·04	6	9	12	20	−2·70	0·04
La	31·0	1·86	2·89	77·8	69·0	60·2	37·2	3·98	2·91
Ce	62·2	1·46	2·52	137·9	123·7	109·4	71·9	3·26	2·54
Pr	6·58	1·07	2·13†	12·52	11·41	10·29	7·34	2·47	2·17†
Nd	20·9	0·78	1·89	35·8	33·0	30·2	22·7	1·84	1·90
Sm	4·0	−0·02	1·06	4·2	4·2	4·1	4·0	0·01	1·05
Eu	0·07	1·71	2·65	0·17	0·15	0·13	0·09	4·19	2·65
Gd	3·3	−0·58	0·59†	2·2	2·4	2·6	3·1	−1·21	0·56†
Tb	0·5	−0·92	0·27†	0·2	0·3	0·3	0·5	−1·07	0·62†
Dy	3·3	−0·89	0·30	1·5	1·8	2·1	2·9	−1·84	0·28
Ho	0·6	−1·05	0·15†	0·2	0·3	0·4	0·6	−2·30	0·08†
Er	2·0	−0·95	0·24†	0·8	1·0	1·3	1·8	−2·11	0·16†
Tm	0·33	−0·8	0·39†	0·17	0·20	0·23	0·29	−1·41	0·47†
Yb	2·2	−1·11	0·18	0·74	1·01	1·28	1·9	−2·46	0·21
Lu	0·35	−1·04	0·21	0·13	0·17	0·21	0·31	−1·79	0·25

C_i, composition interstitial melt; C_0, composition of parent; F, melt fraction; assuming average 0·35 ±0·15.
*Bulk D_i values calculated from phase proportions for P_{total} = 500 MPa and X_{H_2O} = 0·5 (see text).
†Bulk D_i calculated from element RCV$_i$ and trace- and minor-element lines.

Bishop Tuff. As proposed by Hildreth (2004, 2017) and Hildreth & Wilson (2007), the multi-stage, complex processes that led to the origin of the parental granitic mush most probably involved the influx of mantle-derived basalt into the deep crust (which beneath Long Valley caldera is granitoid to ~32 km depth; Fliedner *et al.*, 2000), inducing partial melting and hybridism/differentiation in the trans-crustal column beneath the caldera. The compositional characteristics of the parental body to the Bishop Tuff derived in this study (Table 5) will provide useful constraints for future numerical models that integrate geochemical data with realistic physical and thermal controls on the detailed mechanisms by which these complex trans-crustal processes occurred.

CONCLUSIONS

Several key conclusions can be drawn from this study, which collectively constrain the origin of various geochemical gradients with temperature, including those for H_2O and CO_2, in the high-SiO_2 rhyolite portion of the Bishop Tuff. The main hypothesis that is proposed and tested is that these gradients developed over a range of melt fractions in a parental granitoid mush because of mineral–melt (and fluid–melt) partitioning between interstitial melt and surrounding crystals (and fluid), involving the same nine mineral phases that are found as phenocrysts in the high-SiO_2 rhyolite portion of the Bishop Tuff. A key underlying assumption is that equilibrium crystallization/melting (vs Rayleigh fractional crystallization/melting) most closely models the element partitioning behavior, owing to the crystal-rich nature of the parental mush. The model is thus independent of whether the crystal-rich parental mush to the Bishop Tuff developed as a result of crystallization or partial melting. The most important major conclusions are enumerated below.

(1) The hypothesis that the twofold or lower variation in trace-element concentrations with temperature in the high-SiO_2 rhyolite portion of the Bishop Tuff developed as a result of segregation of variable interstitial melt fractions from a granitic parental mush was shown to be viable. This was done by constructing relative compatibility values (RCV$_i$), defined as the concentration slope with temperature divided by average concentration for each element i, and demonstrating that they are strongly correlated ($R^2 > 0·9$) with

bulk partition coefficients for each element *i* (bulk D_i) for a specific stoichiometry of the crystallization/melting reaction in the parental mush [i.e. points (2), (3), and (4) below].

(2) Only three accessory minerals in the parental mush (allanite, zircon, and apatite) control the bulk partition coefficients of the REE, as well as Y, Hf, Th, and U. When the RCV_i of these trace elements (Figs. 6 and 7) are combined with published mineral–melt partition coefficients for each element, the best fit for the stoichiometry of the three accessory phases in the crystallization/melting reaction in the parental mush is ~0·09 % allanite, ~0·02 % zircon, and ~0·04 % apatite (Fig. 10). Therefore, the increase in the LREE concentrations (e.g. La, Ce) with increasing temperature in the high-SiO_2 rhyolite portion of the Bishop Tuff (i.e. compatible behavior) reflects the presence of allanite in the parental mush. Allanite not only strongly partitions the LREE, but also constrains temperature (<770–780 °C) during melt segregation from the mush owing to its thermal stability limit (Vazquez *et al*., 2004).

(3) Only three ferromagnesian minerals in the parental mush (biotite, titanomagnetite, ilmenite) control the bulk partition coefficients of the four minor elements, Ti, Fe^{3+}, Fe^{2+}, and Mg, and single trace element Mn. When the RCV_i of the four minor elements (Fig. 5) are combined with published mineral–melt partition coefficients for each element, a best fit for the stoichiometry of these three mineral phases in the melting/crystallization reaction in the parental mush is 1·60 % biotite, 0·42 % titanomagnetite, and 0·34 % ilmenite (Fig. 10). Therefore, the increase in Fe^{3+}/Fe^{T} with temperature in the high-SiO_2 rhyolite portion of the Bishop Tuff reflects the larger bulk partition coefficient for Fe^{3+} relative to that for Fe^{2+} during crystallization/melting in the parental mush, which is due to the higher proportion of the mineral phase with $D_{Fe^{3+}} > D_{Fe^{2+}}$ (0·42 % titanomagnetite) than the phase (0·34 % ilmenite) with $D_{Fe^{3+}}$ slightly less than $D_{Fe^{2+}}$.

(4) Identifying the proportions of quartz (Qz), plagioclase (Pl), and K-feldspar (Kfs) in the crystallization/melting reaction in the parental mush, from which the high-SiO_2 rhyolite portion of the Bishop Tuff was segregated, is equivalent to locating the position of the eutectic in the Qz–Pl–Kfs ternary, which varies as a function of pressure and fluid composition (X_{H_2O}). When bulk partition coefficients for Ba, Sr, Eu, and Rb were calculated for different tectosilicate proportions (utilizing mineral–melt partition coefficient on the basis of published experiments and lattice-strain models; Figs 8 and 9), which vary for different P–$X^{fluid}_{H_2O}$conditions (Holtz *et al*., 1992; Table 4), the best fit to the trace-element linear relationship with RCV_i corresponds to an average melt segregation pressure of ~400–550 MPa and average fluid $X^{fluid}_{H_2O}$ of ~0·4–0·6 (Figs 11 and 12). At these conditions, the stoichiometry of the three tectosilicate phases in the crystallization/melting reaction in the parental, crystal-rich mush is ~32 % quartz, ~34 % plagioclase, and ~31 % K-feldspar.

(5) Temperatures during crystallization/melting in the parental mush are constrained to be ≤770–780 °C owing to the presence of allanite (Vazquez *et al*., 2004). Therefore, the average P–T–$X^{fluid}_{H_2O}$ conditions in the parental mush are constrained, which allows the average concentration of H_2O (~7·2 wt%) and CO_2 (~2269 ppm) in the interstitial melt to be calculated based on their solubilities at these conditions (~750 °C, ~500 MPa, $X^{fluid}_{H_2O}$ ~ 0·5).

(6) Evidence that an excess fluid phase was present in the parental mush is seen in the decreasing versus increasing H_2O and CO_2 contents, respectively, in the high-SiO_2 rhyolite portion of the Bishop Tuff with temperature (i.e. incompatible versus compatible behavior, respectively). Only the presence of a fluid phase, which strongly partitions CO_2 relative to the melt, can explain the compatible behavior of CO_2. However, it must have been relatively low in abundance during crystallization/melting in the parental mush to explain the incompatible behavior of H_2O. Calculated degassing paths at 750 °C between the P–$X^{fluid}_{H_2O}$ conditions during melt segregation (~400–550 MPa and $X^{fluid}_{H_2O}$ ~ 0·4–0·6) and those during phenocryst growth (100–200 MPa; $X^{fluid}_{H_2O}$ >0·9), on the basis of published volatile analyses in quartz-hosted melt inclusions, are fully consistent and constrain fluid abundances to be ≤1 wt% (Fig. 12).

(7) The source of volatiles in the parental mush, irrespective of whether it formed by crystallization or partial melting, is required to be exsolved fluids from associated basaltic sills or dikes, as granitoid crust is too volatile poor. Published constraints on the average water content of Plio-Quaternary basalts erupted adjacent to the Long Valley caldera (~4 wt% H_2O; Jolles & Lange, 2021), together with estimates of their CO_2 contents (~4000 ± 2000 ppm), indicate that the composition of exsolved fluids from these basalts (after complete crystallization where ≤1 wt% may be held in biotite/hornblende) was $X^{fluid}_{H_2O}$ ≥ 0·95 (± 0·02). Mass-balance constraints show that the volume of basalt required to supply the requisite volatiles is approximately twice the volume of the interstitial melt of the parental mush. Thus, ~840 km^3 of basalt is required to supply the volatiles for ~400 km^3 Bishop high-SiO_2 rhyolite.

(8) If the parental mush to the Bishop Tuff formed by partial melting of a granitoid (versus crystallization from a melt), it must have occurred in the presence of a fluid ($X^{fluid}_{H_2O}$ ≥ 0·95) exsolved from newly emplaced basalts, as concluded above. The granitoid solidus in the presence of such a water-rich fluid is ≤700 °C, which is consistent with the presence of allanite (stable only at ≤770–780 °C; Vazquez *et al*., 2004) in the parental mush to the Bishop Tuff over a range of melt fractions. For a fixed mass of fluid derived from the basalts (i.e. not infinitely abundant), its composition is expected to evolve as it progressively dissolves into the partial melt of a granitoid. Owing to the much higher solubility of H_2O relative to CO_2 in the interstitial melt, the fluid composition will change to progressively lower $X^{fluid}_{H_2O}$ values with increasing melt fraction, while the dissolved H_2O and CO_2 concentrations in the melt will decrease and increase, respectively. Melts formed at lower melt fractions (i.e. lower temperatures), namely the Early-type rhyolites, will be relatively H_2O-rich and CO_2-poor, with a fluid composition of $X^{fluid}_{H_2O}$ ~ 0·6–0·5 at the time of melt segregation, whereas those melts formed at progressively higher melt fractions (i.e. higher temperatures), namely Transitional-type rhyolites, will contain less H_2O and more CO_2, with a fluid composition of $X^{fluid}_{H_2O}$ ~ 0·5–0·4 during melt segregation. Thus, progressive partial melting of granitoid, which has interacted with a finite mass of H_2O-rich fluid (exsolved from basalts), is expected to produce an evolving fluid composition in the parental leucogranitic mush, as well as evolving volatile contents in the interstitial melt, as melt fraction increases (Fig. 13).

(9) The derivation of bulk D_i values for all minor and trace elements in Early- and Transitional-type samples from the Bishop Tuff (obtained from best-fit linear relationships with RCV_i) allows the bulk composition of the parental source to be estimated. For a melt fraction of 35 % (±15 %), the immediate parent to the high-SiO_2 rhyolite portion of the Bishop Tuff is shown to have been relatively differentiated, with low Ba (≤123 ppm) and Sr (≤36 ppm) contents. It was also notably enriched in La (≤78 ppm) and Ce (≤138 ppm), which differs from most Mesozoic granitoids in the

Sierra Nevada batholith, including leucogranites. The elevated LREE concentrations point to an origin that included material contributions from the Plio-Quaternary Long Valley basalts, notable for their elevated concentrations of the LREE (Cousens, 1996). This conclusion is consistent with isotopic data from the literature (e.g. Halliday *et al*., 1984; Simon *et al*., 2014) that also demonstrate the material involvement of the Long Valley basalts in the parental source to the Bishop Tuff. Collectively, the results from this study provide constraints for new numerical models of the multi-stage, physical processes, which involved the influx of Plio-Quaternary basalts into the trans-crustal granitoid (≤32 km) crust beneath Long Valley caldera (e.g. Hildreth, 2004, 2017), that led to the development of the parental mush to the high-SiO_2 rhyolite portion of the Bishop Tuff.

(10) The viability of the proposed hypothesis in this study, namely that the geochemical gradients with temperature in the high-SiO_2 rhyolite portion of the Bishop Tuff can be explained by segregations of variable melt fractions from a crystallizing/melting parental mush, requires that the parent was broadly homogeneous in composition and mineral assemblage (modal abundances could have varied, but not the mineral phases present). This precludes the mixing of different melt compositions in a crystallizing reservoir and/or partial melting of two (or more) plutons that had distinctly different compositions and/or mineral assemblages. Therefore, the successful application of this approach to other volcanic deposits depends on whether or not they also, like the high-SiO_2 rhyolite portion of the Bishop Tuff, were derived from a relatively homogeneous parental source.

FUNDING

This work was funded by the National Science Foundation (EAR 1855751), as well as discretionary research accounts from the University of Michigan.

DATA AVAILABILITY STATEMENT

The data underlying this article are available in the article and in its online supplementary material.

ACKNOWLEDGEMENTS

An earlier version of this paper benefited from the constructive and supportive comments provided by Adam Simon and Youxue Zhang. We additionally thank Gordon Moore for his probing questions regarding the origin of the volatile gradients in the Bishop Tuff. In addition, insightful and detailed reviews from Luca Carrichi, Madison Myers, and an anonymous reviewer greatly improved the revised paper and helped us to clarify several points. We are also very grateful to Wes Hildreth for his informal review, which also helped us to further improve the paper and provide clearer explanations of our approach.

REFERENCES

Aigner-Torres, M., Blundy, J., Ulmer, P. & Pettke, T. (2007). Laser ablation ICPMS study of trace element partitioning between plagioclase and basaltic melts: An experimental approach. *Contributions to Mineralogy and Petrology*, **153**, 647–667.

Andersen, N. L., Jicha, B. R., Singer, B. S. & Hildreth, W. (2017). Incremental heating of Bishop Tuff sanidine reveals preeruptive radiogenic Ar and rapid remobilization from cold storage. *Proceedings of the National Academy of Science of the USA*, **114**, 12407–12412.

Anderson, A. T., Davis, A. M. & Lu, F. (2000). Evolution of Bishop Tuff rhyolitic magma based on melt and magnetite inclusions and zoned phenocrysts. *Journal of Petrology*, **41**, 449–473.

Bateman, P. C. & Chappell, B. W. (1979). Crystallization, fractionation and solidification of the Tuolumne intrusive series. Yosemite National Park. *California. Geological Society of America Bulletin*, **90**, 465–482.

Bindeman, I. N. & Davis, A. M. (2000). Trace element partitioning between plagioclase and melt: Investigation of dopant influence of partition behavior. *Geochimica et Cosmochimica Acta*, **64**, 2863–2878.

Bindeman, I. N., Davis, A. M. & Drake, M. J. (1998). An ion microprobe study of plagioclase–basalt partition experiments at natural concentration levels of trace elements. *Geochimica et Cosmochimica Acta*, **62**, 1175–1192.

Blundy, J. D. & Wood, B. J. (1991). Crystal-chemical controls on the partitioning of Sr and Ba between plagioclase feldspar, silicate melts, and hydrothermal solutions. *Geochimica et Cosmochimica Acta*, **55**, 193–209.

Blundy, J. D. & Wood, B. J. (1994). Prediction of crystal–melt partition coefficients from elastic moduli. *Nature*, **372**, 452–454.

Calogero, M. A., Hetland, E. A. & Lange, R. A. (2020). High-resolution numerical modeling of heat and volatile transfer from basalt to wall rock: Application to the crustal column beneath Long Valley Caldera, CA. *Journal of Geophysical Research: Solid Earth*, **125**, e2018JB016773.

Carmichael, I. S. E. (1991). The redox states of basic and silicic magmas: A reflection of their source regions? *Contributions to Mineralogy and Petrology*, **106**, 129–141.

Chamberlain, K. J., Morgan, D. J. & Wilson, C. J. N. (2014). Timescales of mixing and mobilisation in the Bishop Tuff magma body: perspectives from diffusion chronometry. *Contributions to Mineralogy and Petrology*, **168**, 1034.

Chamberlain, K. J., Wilson, C. J. N., Wallace, P. J. & Millet, M. A. (2015). Micro-analytical perspectives on the Bishop Tuff and its magma chamber. *Journal of Petrology*, **56**, 605–640.

Coleman, D. S., Bartlet, J. M., Glazner, A. F. & Pardue, M. J. (2012). Is chemical zonation in plutonic rocks driven by changes in source magma composition or shallow-crustal differentiation? *Geosphere*, **8**, 1568–1587.

Cousens, B. L. (1996). Magmatic evolution of Quaternary mafic magmas at Long Valley Caldera and the Devils Postpile, California: Effects of crustal contamination on lithospheric mantle-derived magmas. *Journal of Geophysical Research*, **101**, 27673–27689.

Davies, G. R. & Halliday, A. N. (1998). Development of the Long Valley rhyolitic magma system: Strontium and neodymium isotope evidence from glasses and individual phenocrysts. *Geochimica et Cosmochimica Acta*, **62**, 3561–3574.

Davies, G. R., Halliday, A. N., Mahood, G. A. & Hall, C. M. (1994). Isotopic constraints on the production rates, crystallization histories and residence times of pre-caldera silicic magmas, Long Valley, California. *Earth and Planetary Science Letters*, **125**, 17–37.

Dohmen, R. & Blundy, J. (2014). A predictive thermodynamic model for element partitioning between plagioclase and melt as a function of pressure, temperature, and composition. *American Journal of Science*, **314**, 1319–1372.

Dufek, J. & Bachmann, O. (2010). Quantum magmatism: Magmatic compositional gaps generated by melt–crystal dynamics. *Geology*, **38**, 687–690.

Ebadi, A. & Johannes, W. (1991). Beginning of melting and composition of first melts in the system Qz–Ab–Or–H_2O–CO_2. *Contributions to Mineralogy and Petrology*, **106**, 286–295.

Evans, B. W., Hildreth, W., Bachmann, O. & Scaillet, B. (2016). In defense of magnetite–ilmenite thermometry in the Bishop Tuff and its gradients in silicic magma reservoirs. *American Mineralogist*, **101**, 469–482.

Fliedner, M. M., Klemperer, S. L. & Christensen, N. I. (2000). Three-dimensional seismic model of the Sierra Nevada arc, California, and implications for crustal and mantle composition. *Journal of Geophysical Research*, **105**, 10899–10922.

Ghiorso, M. & Evans, B. W. (2008). Thermodynamics of rhombohedral oxide solutions and revision of the Fe–Ti two-oxide geothermometer and oxygen barometer. *American Journal of Science*, **308**, 957–1039.

Ghiorso, M. S. & Sack, R. O. (1991). Fe–Ti oxide geothermometry: Thermodynamic forumulation and the estimation of intensive variables in silicic magmas. *Contributions to Mineralogy and Petrology*, **108**, 485–510.

Glazner, A. F., Coleman, D. S. & Bartley, J. M. (2008). The tenuous connection between high-silica rhyolites and granodiorite plutons. *Geology*, **36**, 183–186.

Glazner, A. F., Bartley, J. M., Coleman, D. S. & Lindgren, K. (2020). Aplite diking and infiltration: A differentiation mechanism restricted to plutonic rocks. *Contributions to Mineralogy and Petrology*, **175**, 37.

Gualda, G. A. R., Ghiorso, M. S., Lemons, R. V. & Carley, T. L. (2012). Rhyolite-MELTS: A modified calibration of MELTS optimized for silica-rich, fluid-bearing magmatic systems. *Journal of Petrology*, **53**, 875–890.

Guo, X., Lange, R. A. & Ai, Y. (2014). Density and sound speed measurements on model basalt (An–Di–Hd) liquids at one bar: New constraints on the partial molar volume and compressibility of the FeO component. *Earth and Planetary Science Letters*, **388**, 283–292.

Halliday, A. N., Fallick, A. E., Hutchinson, J. & Hildreth, W. (1984). A Nd, Sr, and O isotopic investigation into the causes of chemical and isotopic zonation in the Bishop Tuff. *California. Earth and Planetary Science Letters*, **68**, 379–391.

Hanchar, J. M. & Watson, E. B. (2003). Zircon saturation thermometry. In Hanchar, J. M. & Hoskin, P. W. O., (eds) *Mineralogical Society of America and Geochemical Society, Reviews in Mineralogy and Geochemistry*, **53**, 89–112.

Hervig, R. L. & Dunbar, N. W. (1992). Cause of chemical zoning in the Bishop (California) and Bandelier (New Mexico) magma chambers. *Earth and Planetary Science Letters*, **11**, 97–108.

Hildreth, E. W. (1977). *The magma chamber of the Bishop Tuff: gradients in temperature, pressure, and composition*. PhD thesis, University of California, Berkeley,

Hildreth, W. (1979) The Bishop Tuff: evidence for the origin of compositional zonation in silicic magma chambers. In: (Chapin C. E. & Elston W. E. (eds)) *Ash-flow Tuffs. Geological Society of America, Special Papers*, Vol. **180**, pp. 43–75.

Hildreth, W. (2004). Volcanological perspectives on Long Valley, Mammoth Mountain, and Mono Craters: several contiguous but discrete systems. *Journal of Volcanology and Geothermal Research*, **136**, 169–198.

Hildreth, W. (2017) In: (Hildreth W. & Fierstein J. (eds)) *A refreshing overview of the Bishop Tuff*, *Geologic field-trip guide to Long Valley Caldera, California*, *US Geological Survey, Scientific Investigations Report* **2017-5022-L**, 75–87.

Hildreth, W. & Wilson, C. J. N. (2007). Compositional zoning of the Bishop Tuff. *Journal of Petrology*, **48**, 934–952.

Holtz, F., Behrens, H., Dingwell, D. B. & Taylor, R. P. (1992). Water solubility in aluminosilicate melts of haplogranite composition at 2 kbar. *Chemical Geology*, **96**, 289–302.

Johannes, W. (1984). Beginning of melting in the granite system Qz–Or–Ab–An–H_2O. *Contributions to Mineralogy and Petrology*, **86**, 264–273.

Johannes, W. & Holtz, F. (1996) *Petrogenesis and Experimental Petrology of Granitic Rocks: Minerals and Rock Series*. Berlin: Springer.

Jolles, J. S. R. & Lange, R. A. (2019). High-resolution Fe–Ti oxide thermometry applied to single-clast pumices from the Bishop Tuff: A re-examination of compositional variations in phenocryst phases with temperature. *Contributions to Mineralogy and Petrology*, **174**, 70.

Jolles, J. S. R. & Lange, R. A. (2021). Temperatures and water contents of Long Valley, CA basalts: Application of olivine–melt thermometry and hygrometry at the liquidus. *Journal of Volcanology and Geothermal Research*, **417**, 107298.

Klimm, K., Holtz, F. & Ling, P. L. (2008). Fractionation vs magma mixing in the Wangrah Suite A-type granites, Lachlan Fold Belt, Australia: Experimental constraints. *Lithosphere*, **102**, 415–434.

Kress, V. & Carmichael, I. S. E. (1991). The compressibility of silicate liquids containing Fe_2O_3 and the effect of composition, temperature, oxygen fugacity and pressure on their redox states. *Contributions to Mineralogy and Petrology*, **108**, 82–92.

Lagache, M. & Dujon, S. C. (1987). Distribution of strontium between plagioclases and 1 molar aqueous chloride solutions at 600 °C, 1·5 kbar and 750 °C, 2 kbar. *Bulletin de Minéralogie*, **110**, 551–561.

Lange, R. A. (1997). A revised model for the density and thermal expansivity of K_2O–Na_2O–CaO–MgO–Al_2O_3–SiO_2 liquids between 701 and 1896 K: Extension to crustal magmatic temperatures. *Contributions to Mineralogy and Petrology*, **125**, 277–292.

Lange, R. A. & Carmichael, I. S. E. (1987). Densities of K_2O–Na_2O–CaO–MgO–FeO–Fe_2O_3–Al_2O_3–TiO_2–SiO_2 liquids: New measurements and derived partial molar properties. *Geochimica et Cosmochimica Acta*, **51**, 2931–2946.

Mahood, G. & Hildreth, W. (1983). Large partition coefficients for trace elements in high-silica rhyolites. *Geochimica et Cosmochimica Acta*, **47**, 11–30.

Metz, J. M. & Mahood, G. A. (1991). Development of the Long Valley, California, magma chamber recorded in precaldera rhyolite lavas of Glass Mountain. *Contributions to Mineralogy and Petrology*, **106**, 379–397.

Myers, M. L., Wallace, P. J. & Wilson, C. J. N. (2019). Inferring magma ascent timescales and reconstructing conduit processes in explosive rhyolitic eruptions using diffusive losses from hydrogen from melt inclusions. *Journal of Volcanology and Geothermal Research*, **369**, 95–112.

Newman, S. & Lowenstern, J. B. (2002). VolatileCalc: A silicate melt–H_2O–CO_2 solution model written in Visual Basic for Excel. *Computers & Geosciences*, **28**, 597–604.

Ochs, F. A. & Lange, R. A. (1999). The density of hydrous magmatic liquids. *Science*, **283**, 1314–1317.

Onuma, N., Higuchi, H., Wakita, H. & Nagasawa, H. (1968). Trace element partition between two pyroxenes and the host lava. *Earth and Planetary Science Letters*, **5**, 47–51.

Peppard, T., Steele, I. M., Davis, A. M., Wallace, P. J. & Anderson, A. T. (2001). Zoned quartz phenocrysts from the rhyolitic Bishop Tuff. *American Mineralogist*, **86**, 1034–1052.

Piwinskii, A. J. & Wyllie, P. J. (1968). Experimental studies of igneous rock series: A zoned pluton in the Wallowa Batholith, Oregon. *Journal of Geology*, **76**, 205–234.

Putirka, K. D. (2008). Thermometers and barometers for volcanic systems. In Putirka, K. D. & Tepley, F. J. III, (eds) *Mineralogical Society of America and Geochemical Society, Reviews in Mineralogy and Geochemistry*, **69**, 61–120.

Roberge, J., Wallace, P. J. & Kent, A. J. R. (2013). Magmatic processes in the Bishop Tuff rhyolitic magma based on trace elements in melt inclusions and pumice matrix glass. *Contributions to Mineralogy and Petrology*, **165**, 237–257.

Simon, J. I., Weis, D., DePaolo, D. J., Renne, P. R., Mundil, R. & Schmitt, A. K. (2014). Assimilation of preexisting Pleistocene intrusions at Long Valley by periodic magma recharge accelerates rhyolite generation: Rethinking the remelting model. *Contributions to Mineralogy and Petrology*, **167**, 955.

Sisson, T. W., Ratajeski, K., Hankins, W. B. & Glazner, A. F. (2005). Voluminous granitic magmas from common basaltic sources. *Contributions to Mineralogy and Petrology*, **148**, 635–661.

Tepley, F. J., Lundstrom, C. C. & McDonough, W. F. (2010). Trace element partitioning between high-An plagioclase and basalt to basaltic andesite melt at 1 atmosphere pressure. *Lithos*, **118**, 82–94.

Vander Auwera, J., Longhi, J. & Duchesne, J. C. (2000). The effect of pressure on D_{Sr} (plag/melt) and D_{Cr} (opx/melt): Implications for anorthosite petrogenesis. *Earth and Planetary Science Letters*, **178**, 303–314.

Vazquez, J. A., Manning, C. E., & Reid, M. R. (2004). Experimental determination of allanite stability in high-SiO_2 rhyolite. American Geophysical Union, Fall Meeting 2004, abstract V41C-1407.

Wallace, P. (2005). Volatiles in subduction zone magmas: Concentrations and fluxes based on melt inclusion and volcanic gas data. *Journal of Volcanology and Geothermal Research*, **140**, 217–240.

Wallace, P. J., Anderson, A. T. & Davis, A. M. (1999). Gradients in H_2O, CO_2, and exsolved gas in a large-volume silicic magma system: Interpreting

the record preserved in melt inclusions from the Bishop Tuff. *Journal of Geophysical Research*, **104**, 20097–20122.

Waters, L. E. & Lange, R. A. (2015). An updated calibration of the plagioclase–liquid hygrometer–thermometer applicable to basalts through rhyolites. *American Mineralogist*, **100**, 2172–2184.

Wilson, C. J. N. & Hildreth, W. (1997). The Bishop Tuff: New insights from eruptive stratigraphy. *Journal of Geology*, **105**, 407–439.

Wolff, J. A. & Ramos, R. C. (2013). Processes in caldera-forming high-silica rhyolite magma: Rb–Sr and Pb isotope systematics of the Otowi Member of the Bandelier Tuff, Valles Caldera, New Mexico. *Journal of Petrology*, **55**, 345–375.

Wolff, J. A., Ellis, B. S., Ramos, F. C., Starkel, W. A., Boroughs, S., Olin, P. H. & Bachmann, O. (2015). Remelting of cumulates as a process for producing chemical zoning in silicic tuffs: A comparison of cool, wet and hot, dry rhyolitic magma systems. *Lithos*, **236–237**, 275–286.